Title

Visuomotor experience induces functional and structural plasticity of chandelier cells

Authors

Koen Seignette[1], Nora Jamann[2,3], Paolo Papale[4], Huub Terra[1], Ralph P. O. Porneso[1], Leander de Kraker[1], Chris van der Togt[1,4], Maaike van der Aa[1], Paul Neering[1,4], Emma Ruimschotel[1], Pieter R. Roelfsema[4,5,6,7], Jorrit S. Montijn[8], Matthew W. Self[4], Maarten H. P. Kole[2,3] & Christiaan N. Levelt[1,9,*]

Affiliations

1. Department of Molecular Visual Plasticity, Netherlands Institute for Neuroscience, Meibergdreef 47, 1105 BA Amsterdam, the Netherlands.
2. Department of Axonal Signaling, Netherlands Institute for Neuroscience, Meibergdreef 47, 1105 BA Amsterdam, the Netherlands.
3. Cell Biology, Neurobiology and Biophysics, Department of Biology, Faculty of Science, Utrecht University, Utrecht, The Netherlands.
4. Department of Vision & Cognition, Netherlands Institute for Neuroscience, Meibergdreef 47, 1105 BA Amsterdam, the Netherlands.
5. Laboratory of Visual Brain Therapy, Sorbonne Université, Institut National de la Santé et de la Recherche Médicale, Centre National de la Recherche Scientifique, Institut de la Vision, Paris F-75012, France.
6. Department of Integrative Neurophysiology, Centre for Neurogenomics and Cognitive Research, VU University, Amsterdam, The Netherlands.
7. Department of Psychiatry, Academic Medical Center, University of Amsterdam. Amsterdam, The Netherlands.
8. Department of Cortical Structure & Function, Netherlands Institute for Neuroscience, Meibergdreef 47, 1105 BA Amsterdam, the Netherlands.
9. Department of Molecular and Cellular Neurobiology, Center for Neurogenomics and Cognitive Research, VU University Amsterdam, de Boelelaan 1085, 1081 HV Amsterdam, the Netherlands.

*Correspondence: (c.levelt@nin.knaw.nl)

Abstract

Detailed characterization of interneuron subtypes in primary visual cortex (V1) has greatly contributed to understanding visual perception, yet the role of chandelier cells (ChCs) in visual processing remains poorly characterized. Using viral tracing we found that V1 ChCs predominantly receive monosynaptic input from local layer 5 pyramidal cells and higher-order cortical regions. Two-photon calcium imaging and convolutional neural network modelling revealed that ChCs are visually responsive but weakly selective for stimulus content. In mice running in a virtual tunnel, ChCs respond strongly to locomotion and halting visual flow, suggesting arousal-related activity. Visuomotor experience in the tunnel diminished visual responses of ChCs and induced structural plasticity of ChC boutons and axon initial segment length. Finally, ChCs only weakly inhibited pyramidal cells. These findings suggest that ChCs provide an arousal-related signal to layer 2/3 pyramidal cells that may modulate their activity and/or gate plasticity of their axon initial segments during behaviorally relevant events.

MAIN TEXT

Introduction

The neocortex contains a diverse set of inhibitory interneuron subtypes. The characterization of their connectivity and functions has greatly contributed to our comprehension of cortical circuits and their role in visual perception. The realization that disinhibitory circuits can regulate visual responses based on context has helped to understand mechanisms underlying attention, visual segmentation, predictive processing and plasticity (*1*–*10*). While most cortical interneuron subsets in primary visual cortex (V1) are well-characterized, much remains unknown about the axo-axonic chandelier cells (ChCs) (*11*, *12*) due to the difficulty of genetically targeting them. The recent discovery that vasoactive intestinal peptide receptor 2 (Vipr2) is a marker for cortical ChCs and the availability of Vipr2-Cre mice have now made it possible to perform thorough analyses of this enigmatic cell type (*13*, *14*).

ChCs are unique among interneuron subtypes in that they exclusively innervate pyramidal cells (PyCs) at their axon initial segment (AIS), the site where action potentials are generated (*15*, *16*). This anatomical organization has led to the idea that ChCs may exert powerful control over action potential (AP) generation (*17*). However, there is considerable controversy about whether ChC innervation of the AIS causes inhibition or excitation of PyCs (*17*–*25*). A recent study found that ChCs in primary somatosensory cortex (S1) depolarize the AIS during the first 2-3 weeks after birth, while they cause hyperpolarization or shunting in adult mice (*18*). Accordingly, the few studies that have manipulated ChC activity in adult mice *in vivo* also found an inhibitory effect on PyCs (*26*, *27*).

On top of the limited understanding of their impact on neuronal excitability, there is also little know about the connectivity of ChCs in V1 and their response properties (*28*). In prelimbic cortex, ChCs receive input from local and contralateral PyCs in deep layer 3, while they preferentially innervate more superficial amygdala-innervating PyCs (*26*). This non-reciprocal connectivity pattern suggests that ChCs may shape communication hierarchies between cortical networks. Interestingly, superficial layer 2/3 (L2/3) PyCs in V1 also receive more ChC synapses than deep layer 3 PyCs (*13*), but whether connections are non-reciprocal remains unknown. Recent studies using *in vivo* two-photon calcium imaging in V1 show that ChC activity is highly correlated with pupil size and locomotion (*13*, *29*), indicating arousal-related ChC activity consistent with what has been observed in other brain regions (*27*, *30*, *31*). However, visually evoked activity has also been observed in V1 ChCs (*29*). This activity profile is similar to that of vasoactive intestinal peptide (VIP)+ interneurons and neurogliaform cells (*29*), which are both known to receive strong top-down inputs from higher-order cortical areas. It is not known whether this is also true for ChCs, but if so, an interesting possibility would be that ChCs shape the communication hierarchy of cortical networks providing visual and contextual information.

ChCs have also been implicated in regulating various forms of plasticity. In S1, it was found that ChCs alter the number of synapses at the AIS based on the activity of their postsynaptic targets, suggesting that ChCs may play a role in homeostatic control of PyC activity (*18*). A contribution to homeostatic scaling of neuronal output is consistent with the observation that the size of the PyC soma is proportional with the number of ChC synaptic contacts (*13*, *17*). Furthermore, in CA1 it was discovered that optogenetic suppression of ChCs during spatial

exploration favors place field remapping (*27*). Finally, in the binocular zone of developing V1, elimination of ChCs during development was found to be crucial for the maturation of inputs from the ipsilateral eye and depth perception (*32*). Together, these studies suggest that ChCs may regulate plasticity by directly altering the excitability of their targets at the AIS or reducing the ability of PyCs to undergo changes of their excitatory synaptic inputs.

Here, we analyzed ChCs in L2/3 of V1 to understand their role in visual processing and plasticity. We find that ChCs receive inputs from local L5 PyCs and higher cortical regions and exhibit weak selectivity for visual stimulus content. Imaging ChC activity in mice running through a virtual tunnel showed that they respond to locomotion and visuomotor mismatch, indicating arousal-related activity. Surprisingly, visuomotor experience in the virtual tunnel strongly decreased ChC visual responses. It also resulted in plasticity of the length of PyC AISs and their innervation by ChCs. Finally, ChCs exerted only mild inhibitory influence on PyCs. Our findings suggest that ChCs predominantly respond to arousal related to locomotion or unexpected events/stimuli, and act to modulate activity or plasticity of L2/3 PyCs in V1.

Results

ChCs receive input from long-range sources and L5 PyCs in V1

We first identified the sources of synaptic input to ChCs in V1 using trans-synaptic retrograde rabies tracing. In order to label ChCs in layer 2/3, we made use of Vipr2-Cre mice, in which Cre recombinase is selectively expressed in cortical ChCs (*13*, *14*, *33*). In superficial V1 of these mice, we injected Cre-dependent AAV vectors expressing the avian glycoprotein EnvA receptor TVA and rabies glycoprotein (G) on day 1, followed by a glycoprotein-deleted (dG) rabies virus on day 27 (*34*) (**Fig. 1A,B**). Most labeled neurons were located on the border between L1 and L2/3 and displayed typical ChC morphology (**Fig. S1A,B**). Quantification based on morphological properties revealed that 87% (287/329) of labeled neurons were ChCs. (**Fig. S1A,B)**. This specificity matches that of Cre driver lines for other inhibitory subtypes (*35*). We tested the specificity of the rabies virus by injecting it without the AAV helper vectors and found no labeled neurons (**Fig. S1C**). We then quantified neurons providing monosynaptic input to ChCs across the brain of four mice also injected with the AAV helper vectors. This revealed that ChCs received long-range inputs from various thalamic and cortical regions (e.g., dorsal lateral geniculate nucleus, lateral posterior nucleus, retrosplenial cortex, and S1), matching long-range inputs described for other interneuron subsets in V1 (*36*). The most abundant sources of presynaptic partners of ChCs, however, were found locally in L5 and to a lesser extent in L1-4 of V1 (**Fig. 1C**). Labeled L5 neurons had pyramidal shaped cell bodies and dendritic spines, indicating that L5 inputs to ChCs are excitatory (**Fig. S1D-F**). This local innervation pattern was reminiscent of ChCs in S1 (*37*), but differed significantly from the innervation pattern of ChCs in the prefrontal cortex where they predominantly receive input from contralaterally-projecting PyCs in deep layer 3 (*26*).

To test the monosynaptic nature of the long-range input cells observed with rabies tracing, we used optogenetic stimulation in combination with electrophysiological recordings in acute V1 slices. For these experiments we injected an AAV vector driving expression of ChR2-eYFP in retrosplenial cortex for optogenetic stimulation. This area

was chosen because it contained more input neurons than any other brain area that was sufficiently distal from V1 to prevent potential leakage of the viral vector into V1 itself. We also injected a Cre-dependent AAV vector driving mCyRFP1 expression in V1 to label ChCs and performed whole-cell recordings in V1 slices three weeks later (**Fig. 1D-F**). Local optogenetic activation of RSC boutons in V1 generated inward currents in ~85% (11/13) of voltage-clamped ChCs. The resulting excitatory postsynaptic potentials were abolished in the presence of tetrodotoxin (TTX), but reappeared upon additional application of the potassium-channel blocker four-aminopyridine (4-AP) (**Fig. 1H**), which facilitates optogenetically evoked synaptic release in absence of action potential generation. These data corroborate the idea that RSC inputs onto V1 ChCs are monosynaptic (*38*). Repeated optogenetic stimulation (20 Hz) resulted in synaptic depression (**Fig. 1I**), indicating RSC synapses may have a high release probability (*39*).

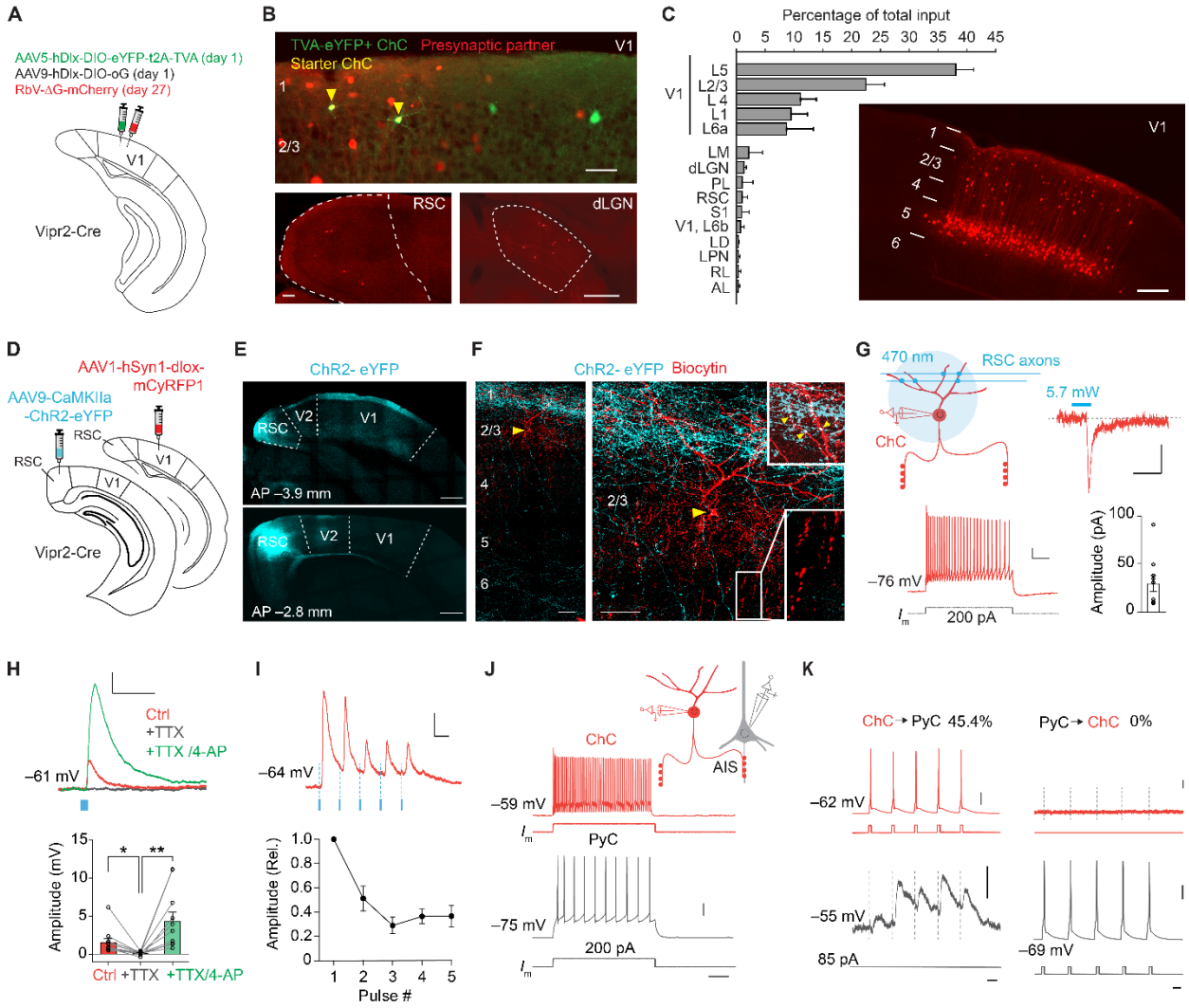

Figure 1. ChCs receive input from L5 PyCs and innervate L2/3 PyCs

(A) Schematic with viral strategy for selective monosynaptic retrograde rabies tracing of L2/3 ChCs.

(B) Overview of superficial V1 region (top) with starter ChCs (yellow), non-starter ChCs (green) and presynaptic partners (red). Scale bar, 50 µm. Bottom: example images of RSC (left; scale bar, 100 µm) and dLGN (right; scale bar, 200 µm) containing input cells in red. Number of starter ChCs = 7.5 +- 3.8 (mean +- SEM, with a total of 30 starter ChCs from 4 mice).

(C) Quantification of input sources to ChCs (n = 4 mice) represented as percentage (mean +- SEM) of the total number of presynaptic neurons observed brain wide. LM, lateromedial visual area; dLGN, dorsal lateral

geniculate nucleus; PL, posterolateral visual area; RSC, retrosplenial cortex; S1, primary somatosensory area; LD, lateral dorsal nucleus of the thalamus; LPN, lateral posterior nucleus of the thalamus; RL, rostrolateral area; AL, anterolateral visual area. The image shows the distribution of input neurons selectively within V1. Scale bar, 200 µm.

(D) Schematic with viral strategy for optogenetic activation of RSC inputs to L2 ChCs. PyCs in RSC were labeled with ChR2-eYFP, ChCs in V1 were labeled with the red fluorophore mCyRFP1.

(E) Confocal images showing the ChR2-eYFP (cyan) injection location in RSC (bottom) and their projections to L1 in V1 (top). Scale bar, 500 µm.

(F) Confocal images of the biocytin fill (red) of mCyRFP+ neurons revealed L2 ChC identity. Insets depict putative RSC inputs on apical dendrites of ChC in layer 1 (cyan, top) as well as characteristic rows of ChC bouton cartridges (bottom). Yellow arrow indicates soma. Scale bars, 50 µm.

(G) Schematic of whole-cell patch-clamp recordings from mCyRFP+ neurons. Current injections evoked firing patterns characteristic of ChCs. Scale bars, 10 mV, 100 ms. Optogenetic activation of RSC boutons evoked inward currents of on average 29.8 pA (n = 11/13 ChC). Bar shows mean and SEM, dots individual cells. Scale bars, 20 ms, 10 pA.

(H) TTX/4-AP bath application confirmed monosynaptic RSC (470 nm optogenetically evoked, blue) inputs in ChCs. RM ANOVA **p = 0.0035, Holm-Šídák's multiple comparisons test, *p = 0.012, **p = 0.008. Bar shows mean +- SEM, dots represent individual cells, n = 11. Scale bars, 1 mV, 100 ms

(I) Optogenetic stimulation at 20 Hz revealed a reduction in postsynaptic potential amplitudes. Circles show mean +- SEM. Scale bars, 2 mV, 50 ms.

(J) Voltage responses to a current injection steps in ChCs and PyCs during simultaneous recordings. Scale bars, 100 ms, 20 mV.

(K) Action potentials were generated by brief current injections in ChCs (left) or PyCs (right). In n = 5 out of 11 pairs, ChC stimulation generated postsynaptic responses in PyCs. In n = 0/11 PyC were projecting back onto ChC. Scale bars 10 ms, 20 mV, and 0.5 mV for subthreshold responses, n = 6 mice.

Finally, we performed paired recordings of L2/3 PyCs and ChCs to test their local connectivity within V1 (**Fig. 1J-K**). Inducing action potentials in ChCs generated postsynaptic responses in ~45% (5/11) of PyCs. However, none of the 11 ChCs we recorded from responded to local PyC stimulation (**Fig. 1J-K**), indicating a highly non-reciprocal connectivity motif. It also indicated that only few if any local L2/3 PyCs provide synaptic input to ChCs. It should be noted that the use of whole cell recordings with high chloride internal solution as performed here precludes determining whether ChC input on PyCs causes hyperpolarization or depolarization. These findings suggest that the rabies-labeled L1-4 neurons providing monosynaptic input to ChCs are predominantly inhibitory neurons, in line with previous work showing that V1 ChCs receive local input from L2/3 SST+ interneurons as well as neurogliaform cells (L2/3 NGCs), but not from L2/3 PyCs (*40*). This is further supported by the distributed localization of the labeled neurons, their presence in L1 and the observation that they lacked spines and that the soma appeared non-pyramidal (**Fig. S1D-F**). Taken together, these results show that ChCs in V1 receive substantial input from local L5 PyCs, inhibitory neurons and long-range sources, while they locally innervate L2/3 PyCs.

Chandelier cells are modulated by arousal and show high correlations

Having studied their connectivity, we next looked at the *in vivo* response properties of ChCs and L2/3 PyCs using two-photon calcium imaging in awake animals. We injected adult Vipr2-Cre mice with an AAV vector driving expression of GCaMP6f under the control of a short CaMKIIa promoter to label putative PyCs and a Cre-dependent AAV vector driving expression of mRuby2-GCaMP6f to label ChCs in V1. We implanted the mice with a cranial window and head ring to allow head fixation on a running wheel (**Fig. 2A**).

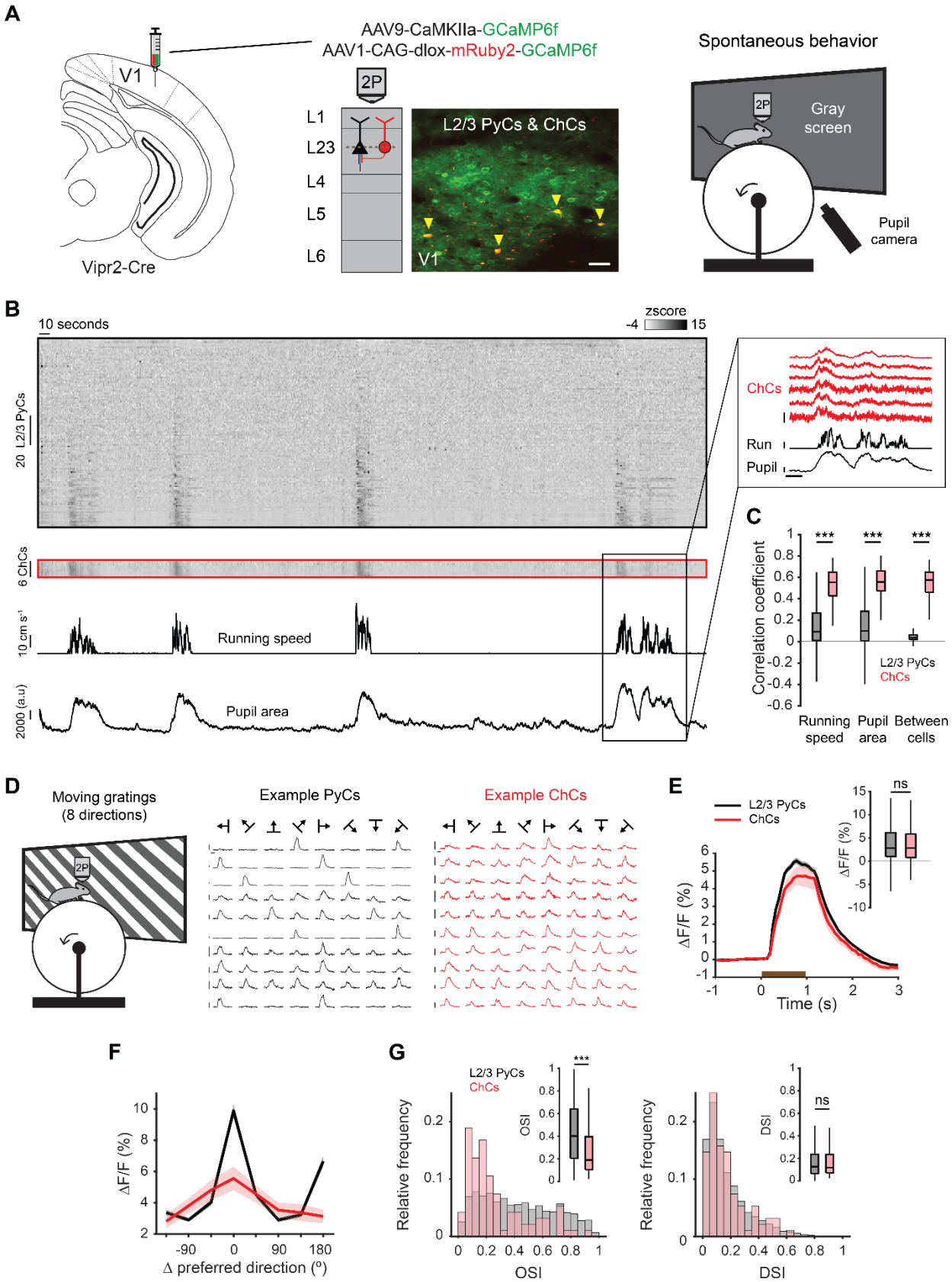
A
V1
Vipr2-Cre
AAV9-CaMKIIa-GCaMP6f
AAV1-CAG-dlox-mRuby2-GCaMP6f
2P
L1
L23
L4
L5
L6
L2/3 PyCs & ChCs
V1
Spontaneous behavior
2P
Gray screen
Pupil camera
B
10 seconds
zscore
-4
15
20 L2/3 PyCs
6 ChCs
10 cm s-1
Running speed
2000 (a.u)
Pupil area
ChCs
Run
Pupil
C
Correlation coefficient
***
L2/3 PyCs
ChCs
Running speed
Pupil area
Between cells
D
Moving gratings (8 directions)
2P
Example PyCs
Example ChCs
E
L2/3 PyCs
ChCs
ΔF/F (%)
Time (s)
ns
F
ΔF/F (%)
Δ preferred direction (°)
G
L2/3 PyCs
ChCs
Relative frequency
OSI
***
DSI
ns

Figure 2. Chandelier cells are modulated by arousal and show high correlations.

(A) Schematic of approach. Chandelier cells (selectively expressing Cre in Vipr2-Cre mice) were identified using the red fluorophore mRuby2 and neuronal activity of ChCs (yellow arrows) as well as L2/3 PyCs was tracked using two-photon calcium imaging of GCaMP6f. Scale bar, 50 µm. Mice were allowed to freely run or rest while viewing a gray screen.

(B) Example recording of PyCs (black box) and ChCs (red box) with tracking of running speed and pupil area (bottom two rows). Single cell ΔF/F traces were z-scored for display purposes. The inset highlights the correlated activity of six ChCs. Inset vertical scale bars, 4 zscore (ChCs), 10 cm/s (run), 2000 a.u. (pupil). Horizontal scale bar, 10 s.

(C) Average correlation coefficients for ΔF/F of PyCs and ChCs with running speed, pupil area and within cell type. ChCs show higher correlation coefficients than PyCs across conditions (15 sessions from 8 mice, n = 1883 PyCs and 95 ChCs, 19 +- 2.93 ChC pairs per field of view). Linear Mixed Effects Model (LMEM) for all comparisons. ***: $p < 0.001$, ns: not significant. Box plots represent median, quantiles and 95% confidence interval (CI) over neurons.

(D) Schematic of recording during visual stimulation with moving gratings (left) and responses to all directions for example PyCs (middle) and ChCs (right). Vertical scale bars, 10% ΔF/F, horizontal scale bars, 1 s.

(E) Average response of L2/3 PyCs and ChCs to moving gratings (1 s, brown bar) and quantification showing no significant differences between PyCs and ChCs (inset, averaged over 0.2-1.2 s after stimulus onset).

(F) Orientation- and direction tuning curves. Curves represent mean +- SEM over neurons after aligning single cell curves to their preferred direction.

(G) Histograms and average OSI and DSI (insets) for L2/3 PyCs and ChCs. ChCs are more weakly tuned to orientation, but not direction of moving gratings than L2/3 PyCs.

We first assessed activity of ChCs and L2/3 PyCs during spontaneous behavior by tracking running speed and pupil size while mice were viewing a uniform gray screen (**Fig. 2A, Movie S1**). We restricted our field of view to the border between L1 and L2/3, where superficial ChCs are positioned. In line with earlier work, correlation analysis between calcium activity and both running speed and pupil size revealed that ChCs were mostly active during states of high arousal, more so than L2/3 PyCs (**Fig. 2B-C**, multilevel statistical analyses were performed using a Linear Mixed Effects Model to account for dependencies in the data and variance between mice, see methods) (*13*, *29*). In addition, ChCs within the same field of view were highly correlated with each other, much more so than L2/3 PyCs (**Fig. 2B-C**), suggesting that ChCs distribute a synchronized signal during high arousal.

To test whether ChCs also responded to visual stimuli, we examined their orientation and direction tuning by showing mice 1 s moving oriented gratings (**Fig. 2D, Movie S2**). Although both ChCs and L2/3 PyCs had strong visual responses, ChCs were weakly tuned and showed a lower orientation selectivity index (OSI) than L2/3 PyCs (**Fig. 2E-G**). The direction selectivity index (DSI) was similar between cell types.

ChCs are weakly selective to visual information

The highly synchronized ChC activity, its correlation with arousal, and the relatively weak orientation tuning of ChCs suggested that while they signal behaviorally relevant events, they may only weakly encode visual stimulus features. To assess this more thoroughly, we assessed the visual response properties of ChCs. Artificial visual stimuli such as oriented gratings can reveal tuning to isolated stimulus parameters. However, experimental constraints limit the number of receptive field properties that can be tested this way. In addition, due to the nonlinear response selectivity of visual neurons, receptive field properties defined using gratings do not always generalize well to natural vision (*41*). Therefore, to obtain a more complete picture of the cells' visual receptive field properties we used natural stimuli in combination with a pre-trained deep convolutional neural network (CNN) to model single-

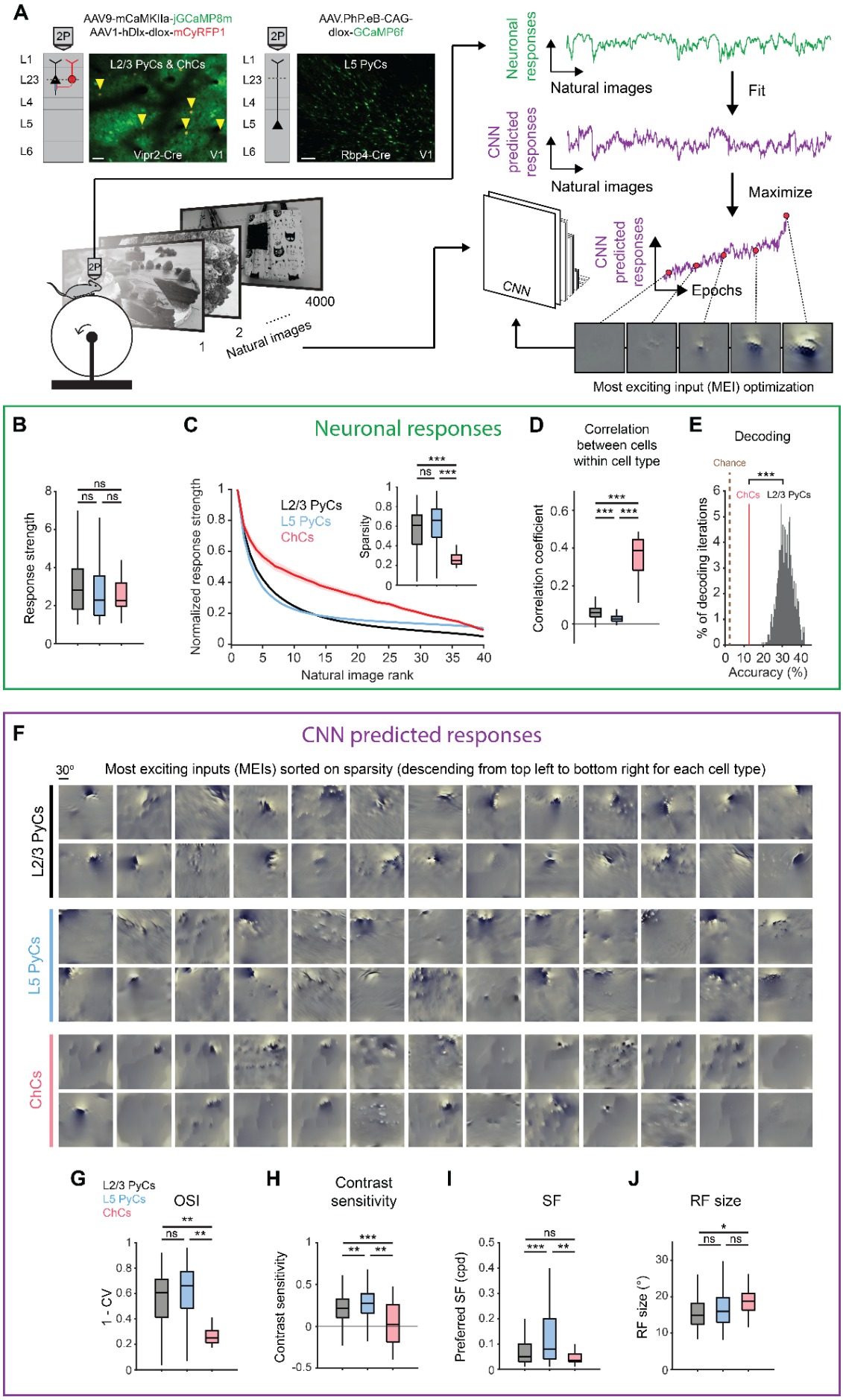
A
AAV9-mCaMKIIa-jGCaMP8m
AAV1-hDlx-dlox-mCyRFP1
AAV.PhP.eB-CAG-dlox-GCaMP6f
2P
L1
L23
L4
L5
L6
L2/3 PyCs & ChCs
Vipr2-Cre
V1
L5 PyCs
Rbp4-Cre
Neuronal responses
Natural images
Fit
CNN predicted responses
Maximize
CNN
Epochs
4000
Natural images
Most exciting input (MEI) optimization
B
Response strength
ns
C
Neuronal responses
Normalized response strength
L2/3 PyCs
L5 PyCs
ChCs
Sparsity
Natural image rank
D
Correlation between cells within cell type
Correlation coefficient
E
Decoding
Chance
ChCs
L2/3 PyCs
% of decoding iterations
Accuracy (%)
F
CNN predicted responses
30°
Most exciting inputs (MEIs) sorted on sparsity (descending from top left to bottom right for each cell type)
L2/3 PyCs
L5 PyCs
ChCs
G
OSI
1 - CV
H
Contrast sensitivity
I
SF
Preferred SF (cpd)
J
RF size
RF size (°)

Figure 3. ChCs are weakly selective to visual information

(A) Schematic of experiment and CNN model fitting. Mice expressing GCaMP8m in L2/3 PyCs and ChCs (Vipr2-Cre mice) or GCaMP6f in L5 PyCs (Rbp4-Cre mice) were shown a set of 4000 images. We trained a CNN to predict single cell responses to a range of visual stimuli and to derive MEIs. Traces (right) represent average responses to natural images (green) and the activity predicted by the CNN (purple) for an example neuron. Scale bars example field of view, 50 µm.

(B) Average response strength to natural images for different neuronal cell types. Box plots represent median, quantiles and 95% confidence interval (CI) over neurons. n = 1015 L2/3 PyCs, 1601 L5 PyCs and 34 ChCs. LMEM for all comparisons, ***: $p < 0.001$, **: $p < 0.01$, *: $p<0.05$, ns: not significant.

(C) Average response strength for different neuronal cell types on a subset of 40 natural images (compared to baseline, see methods). Images are ranked on the strength of the response they elicited for each neuron. ChCs curves are flatter than L2/3 PyCs and L5 PyCs, indicating lower stimulus selectivity. Inset: as in B, but for sparsity (a measure for stimulus selectivity). ChCs have lower sparsity than L2/3 PyCs and L5 PyCs.

(D) As in B, but for correlation during visual stimulation. ChCs have higher within cell type correlations than L2/3 PyCs and L5 PyCs (21 +- 5.08 ChC pairs per field of view, mean +- SEM).

(E) Natural image decoding accuracy for ChCs and L2/3 PyCs. ChC decoding accuracy (red line, 12.55%) was significantly lower than a distribution of decoding accuracies performed using equal numbers of subsampled L2/3 PyCs. Permutation test, ***$p < 0.001$. The brown dotted line indicates theoretical chance level (2.5%).

(F) Single cell most exciting inputs (MEIs) sorted by response sparsity (highest 26 neurons, descending from top left to bottom right). Note the diffuse and unstructured patterns in ChC MEIs.

(G) As in B, but for orientation selectivity (OSI). ChCs have lower OSI than L2/3 PyCs and L5 PyCs.

(H) As in B, but for contrast sensitivity. ChCs have lower contrast sensitivity than L2/3 PyCs and L5 PyCs.

(I) As in B, but for spatial frequency (SF) tuning. ChCs prefer lower SFs than L5 PyCs.

(J) As in B, but for receptive field (RF) size. ChCs have bigger RFs than L2/3 PyCs.

cell visual responses and visualize their putative most exciting inputs (MEIs) (*42–45*) (**Fig. 3**). For this experiment, we used two new groups of mice. In one group, we injected Vipr2-Cre mice with an AAV vector driving expression of GCaMP8m (*46*) (to label L2/3 PyCs and ChCs) and a Cre-dependent AAV vector driving expression of mCyRFP1 (to label ChCs). Since our rabies tracing results revealed that V1 L5 PyCs were the most abundant source of synaptic input to ChCs, we targeted L5 PyCs in a second group of mice. We selectively labeled L5 PyCs using a tail vein injection of a Cre-dependent PhP.eB-serotyped (*47*) AAV vector driving expression of GCaMP6f in Rbp4-Cre mice (*48*) (**Fig. 3A**). We then recorded neural activity in both groups while mice were shown a set of 4000 natural images, with 40 of these images being shown 10 times each. We used the neural responses of individual neurons to determine their selectivity, and subsequently, to optimize a CNN and obtain an estimate of the cells' most exciting inputs (MEIs) (**Fig. 3A**).

We first focused on properties derived from recorded neuronal responses (**Fig. 3B-E and Fig. S2A**). ChCs responded strongly to natural images, comparable to L2/3 PyCs and L5 PyCs (**Fig. 3B**). In order to test the selectivity of neurons for specific natural stimuli, we made use of the subset of 40 images that we presented 10 times. For each cell, we sorted the average responses to these images based on their strength, creating a ranked distribution that revealed differences in stimulus selectivity between cell types (**Fig. 3C**). L2/3 PyCs and L5 PyCs responded strongly to only a few images, indicating high selectivity. In contrast, ChCs were weakly selective as shown by their strong responses to many images. We quantified image selectivity for each neuron by calculating sparsity (*49*). High sparsity indicates strong responses to only a few images, while low sparsity indicates equal responsiveness to many images. As evident from their flattened curve in the ranked distribution, ChCs had significantly lower sparsity than L2/3 PyCs and L5 PyCs (**Fig. 3C, inset**). Next, we reasoned that if ChCs are weakly selective for visual stimuli, their between-cell

correlation should remain high even during exposure to variable visual input. Indeed, correlations between ChCs were considerably higher than those for L2/3 PyCs and L5 PyCs (**Fig. 3D**), similarly to the situation during spontaneous behavior (**Fig. 2C**). Finally, to test whether ChC activity contained less information about the visual stimuli than L2/3 PyC activity, we performed population decoding on the 40 images using linear discriminant analysis (LDA). We compared decoding accuracy using all ChCs (n = 34) with that of a distribution of accuracies obtained from randomly subsampling equal numbers of L2/3 PyCs (see methods). Decoding accuracy of ChCs was significantly lower than of L2/3 PyCs (**Fig. 3E**). Together, these results show that ChCs are visually responsive, but weakly selective to visual information.

While orientation tuning and sparsity are useful measures of selectivity, they do not provide information about the type of stimuli that excite the neurons most strongly. To determine the MEI of each neuron, we used the responses of individual ChCs, L2/3 PyCs and L5 PyCs to optimize a pre-trained CNN (*42–45*). First, we obtained predicted (artificial) responses from the pre-trained CNN to a batch of the natural images. We then fit a mapping function from predicted responses to neuronal responses (recorded from the mice). The mapping function consisted of a set of spatial weights to model the location and spatial extent of the RF and a set of feature weights to model the feature selectivity (e.g. orientation) of each neuron. To fit the model, we compared the neuronal responses with the predicted responses made by the CNN. We repeated this process several times using different batches of natural images. On each iteration, we changed both the spatial and feature weights of the model to minimize the error between neuronal responses and predicted responses, until no further improvements were made. The result of this optimization was the final model, comprising an artificial copy of each individual neuron that could be used to predict visual responses which are highly representative of the neuron's visual response properties (see methods and **Fig. S2B-C**).

The CNN allowed us to obtain an MEI for each neuron by presenting artificial visual stimuli (**Fig. 3F**, see methods) (*43*). MEIs can reveal complex non-linear RF properties such as corners, curves and textures that represent optimal visual input, which is otherwise difficult to quantify in a single metric. Inspection of the MEIs and quantification of predicted responses to simple artificial stimuli revealed striking differences between cell types. For instance, MEIs of L2/3 PyCs often displayed clearly oriented edge-like patterns with sharp ON and OFF regions, which were much less apparent in ChCs (**Fig. 3F**), while L5 PyCs showed a mixed form of selectivity, including both edge-like patterns as well as more complex textures. In line with this observation and in agreement with our orientation tuning experiments (**Fig. 2D-E**), the modeled ChCs had lower OSIs than L2/3 PyCs and L5 PyCs (**Fig. 3G** and **Fig. S2D**). Furthermore, ChC MEIs mostly lacked high contrast patterns, containing high spatial frequencies (SFs). Accordingly, the quantification of contrast tuning and SF of modeled neurons revealed that ChCs were less contrast tuned than L2/3 PyCs and L5 PyCs (**Fig. 3H** and **Fig. S2E**) and preferred lower SFs than L5 PyCs (**Fig. 3I**), which might be related to the interdependence between contrast sensitivity and SFs (*50*, *51*). The smooth and featureless MEIs of ChCs were further reflected by their larger RFs (**Fig. 3J**).

Finally, given that ChCs receive most of their inputs from local L5 PyCs (**Fig. 1C**), we asked whether ChC MEIs could be the result of combinations of L5 PyC inputs. We generated MEIs to maximize the response of combinations of L5 PyCs and found that many of the resulting MEIs were less structured and lacked clearly oriented edge-like patterns (**Fig. S2F**). The similarity of these MEIs with those we found for ChCs is in line with the idea that ChCs are driven by input from large number of L5 PyCs (but do not exclude alternative explanations). Together with the observation that the activity of ChCs is strongly influenced by non-visual factors such as arousal, these results support a view in which ChCs are visually responsive but mostly invariant to the spatial and featural arrangement of visual stimuli.

Locomotion and visuomotor mismatch drive chandelier cell activity in a virtual tunnel

To determine how the interaction between behavior and visual input drives the activity of ChCs, we recorded their calcium responses in V1 of mice in a virtual tunnel paradigm. We designed the tunnel in a way that allowed us to examine L2/3 PyC and ChC activity in response to multiple variables, such as visual stimuli, locomotion and visuomotor mismatch (errors between expected and perceived visual input) (**Fig. 4A-B**). In the first, one-meter-long section of the tunnel ("visual section"), two visual patterns (grating and checker) were repeated three times on a white noise background (**Fig. 4B**, left). The second section ("non-visual") immediately followed the visual section. It consisted of an even, gray area and included an auditory cue predicting a reward (cue at t = 1 s, reward at t = 3 s) and a 6 s waiting period before the next trial started (**Fig. 4B**, right). Mice were trained in a minimum of 6 training sessions, during which they became acquainted to the tunnel and learned to lick for a reward. After training, mice performed the task twice under the two-photon microscope, allowing us to record 1256 PyCs and 38 ChCs from a total of 12 locations in 6 mice (**Fig. 4C**).

ChCs were highly active at the onset of the visual section of the tunnel but became suppressed when the visual stimuli appeared (**Fig. 4C-D** and **Fig. S3A-B**). Interestingly, while a large subpopulation of PyCs were activated by the visual stimuli, many others showed a similar activity profile as ChCs, suggesting functionally separate populations of PyCs (**Fig. 4C**). In order to test this, we performed hierarchical clustering on z-scored average activity in the visual section of the tunnel. We used silhouette analysis to examine the separation distance between clusters for different numbers of clusters, which showed that the optimal number of clusters was two (**Fig. S3C**). Examination of the two clusters of PyCs revealed that they had opposite activity patterns. Cluster 1 was activated by visual stimuli but suppressed in the non-visual section, while cluster 2 was suppressed by visual stimuli but activated in the non-visual section, like ChCs (**Fig. 4C-D**). Thus, we named the PyCs in these clusters 'visually responsive PyCs' (V-PyCs) and 'non-visually responsive PyCs' (NV-PyCs) respectively.

Although the difference between the two clusters was striking, silhouette evaluation cannot rule out a lack of functional clustering: i.e., where the true number of clusters is one. Therefore, to test whether our data were better described by two clusters or one, we compared the separability of the visual response distributions obtained for the real V-PyCs and NV-PyCs to the separability of 1000 random combinations using a permutation test (**Fig. S3C-F**, see methods). The separability between V-PyCs and NV-PyCs was higher than expected by chance (**Fig. S3F**), indicating that V-PyCs and NV-PyCs are functionally separate clusters in our tunnel paradigm.

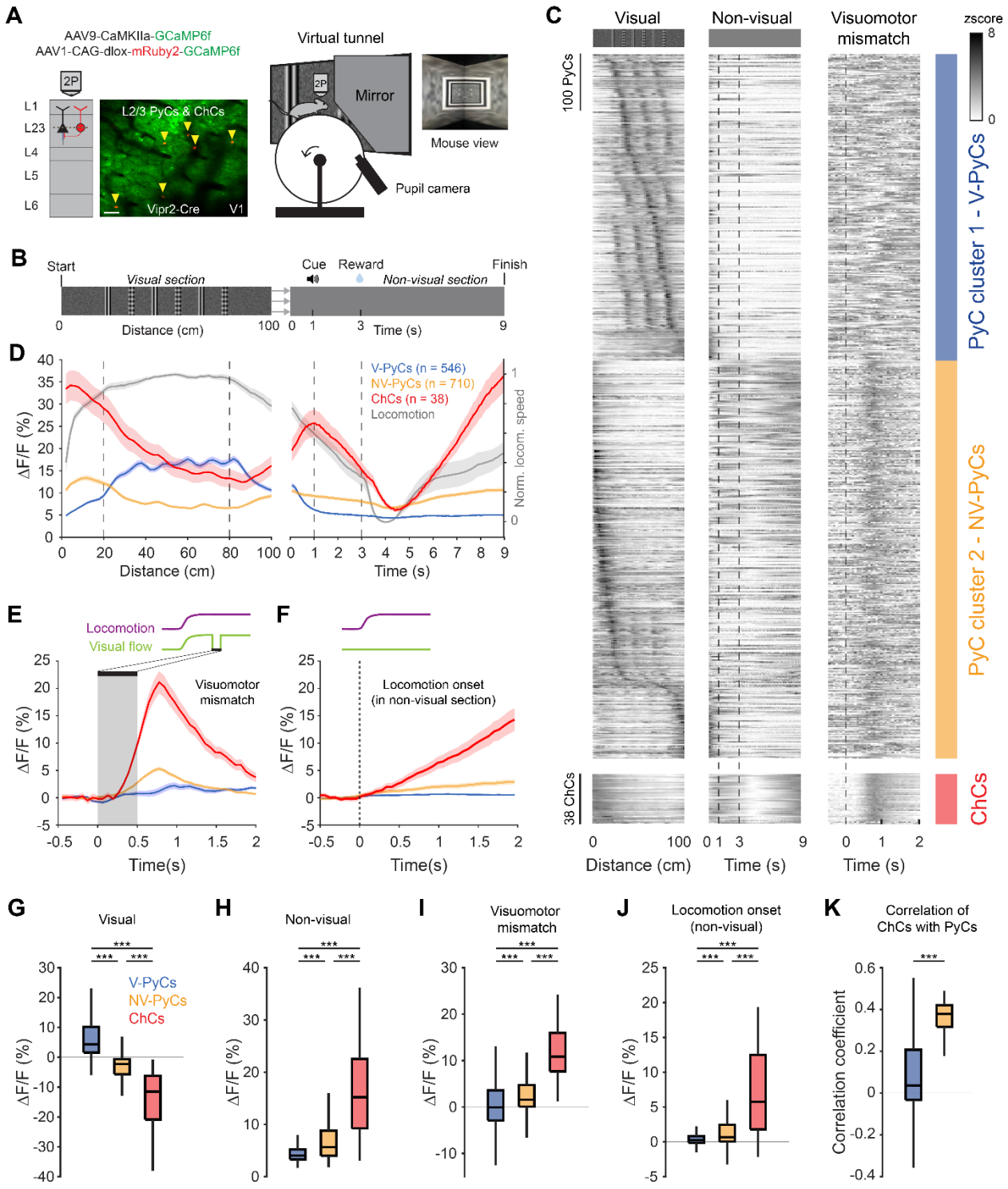

Figure 4. Locomotion and visuomotor mismatch drive chandelier cell activity in a virtual tunnel

(A) Schematic of approach. Vip2r-Cre mice were head-fixed on a running wheel in a visual virtual tunnel. Chandelier cells were identified using the red fluorophore mRuby2 and neuronal activity of ChCs (yellow arrows) as well as PyCs was tracked using two-photon calcium imaging of GCaMP6f. Scale bar, 50 µm.

(B) Virtual tunnel design. Mice ran through a virtual tunnel consisting of a one-meter-long visual section (containing visual stimuli along the walls) immediately followed by a non-visual reward zone in gray screen conditions. In the non-visual section, an auditory cure predicted a water reward two seconds later. After a six second timeout the next trial started.

(C) Single-cell z-scored average activity of all PyCs (blue/orange) and ChCs (red) during visual, non-visual, and visuomotor mismatch parts of the tunnel (n = 1256 PyCs and 38 ChCs, 12 sessions from 6 mice). PyCs were

clustered in two populations using hierarchical clustering based on their z-scored activity in the visual section. Cells are sorted on cluster followed by peak activation location. Note the difference in activity between the visual (cluster 1: V-PyCs, blue) and non-visual (cluster 2: NV-PyCs, orange) PyC populations.

(D) Average population traces of V-PyCs, NV-PyCs and ChCs in the visual (left) and non-visual (right) part of the tunnel. Normalized locomotion speed (right y-axis) is depicted in gray. The ChCs follow the activity profile of NV-PyCs. Traces represent mean +- SEM over neurons for ΔF/F and mean +- SEM over sessions for locomotion speed.

(E) Average population traces during visuomotor mismatch events. NV-PyCs and ChCs show strong mismatch responses.

(F) Average population traces at locomotion onset in the non-visual section of the tunnel. NV-PyCs and ChCs show strong locomotion onset responses.

(G) Average activity during visual stimuli (20-80 cm) compared to start of tunnel (0-20 cm). NV-PyCs and ChCs were strongly suppressed by visual stimuli. Box plots represent median, quantiles and 95% confidence interval (CI) over neurons. LMEM for all comparisons, ***: $p < 0.001$.

(H) As in G, but for activity in the entire non-visual part of the tunnel.

(I) As in G, but for visuomotor mismatch events.

(J) As in G, but for locomotion onset events.

(K) Average correlation coefficient of ChCs with PyCs in visual and non-visual section of the tunnel. ChCs are more strongly correlated with NV-PyCs than V-PyCs.

ChCs have similar response properties as non-visual PyCs

Previous research has demonstrated that a significant fraction of V1 PyCs exhibit strong visuomotor mismatch responses when the visual flow of the tunnel is abruptly stopped while the mice are still running (*7*, *52*–*57*). Recent evidence suggests that PyCs with visuomotor mismatch responses may belong to a genetically distinct subpopulation that is less visually responsive (*52*). Therefore, we assessed whether the two populations of PyCs we identified also differed in terms of their visuomotor mismatch responses. In a subset of trials, we briefly interrupted the visual flow for 0.5 s while the mice were running, to create a visuomotor mismatch. NV-PyCs displayed stronger responses to both the visuomotor mismatch and the onset of running compared to the V-PyCs (**Fig. 4E-F, I-J**). These findings support the idea that different populations of PyCs in L2/3 exist, one primarily responding to visual stimuli and the other to locomotion and visuomotor mismatch.

ChCs showed a similar but more pronounced activity pattern compared to NV-PyCs: they were active at the start of the tunnel, while the visual stimuli in the tunnel suppressed their activity (**Fig. 4C,D,G,H**). Like NV-PyCs, ChCs were mostly driven by locomotion (**Fig. 4F**) and showed strong responses to visuomotor mismatch (**Fig. 4E,I**). In line with this, we found that ChCs were more strongly correlated with NV-PyCs than with V-PyCs (**Fig 4K**).

It is known that a subpopulation of ChCs express parvalbumin (PV) (*58*). Indeed, ChCs in adult V1 can be selectively labeled using the combination of markers Vipr2 and PV (*14*, *29*), but it is not known whether PV^+-ChCs and Vipr2-ChCs (which includes both PV^+ ChCs and PV^- ChCs) are functionally different. We therefore tested whether PV^+ ChCs had similar response properties as Vipr2-ChCs by repeating our tunnel experiments using two Vipr2-Cre X PV-FlpO x AI65(RCFL-tdTom) (*33*) mice (**Fig. S3G**). We found that PV^+-ChCs showed identical activity patterns as Vipr2-ChCs (**Fig. S3H-P**). In addition, in this smaller sample of mice we found the same separation of V-PyCs and NV-PyCs as described in figure 4.

Finally, we assessed the activity of ChCs when visual flow was uncoupled from the running speed of the mouse (open loop condition). This revealed that responses to sudden halts in visual flow that were independent of locomotion were much weaker than responses to closed loop visuomotor mismatch (**Fig. S3Q**). In addition, open loop onset of visual flow when the mouse was not running resulted in a suppression of ChC activity (**Fig. S3Q**). We conclude that in mice trained in our virtual tunnel paradigm, ChCs responded predominantly to locomotion and visuomotor mismatch when visual flow stopped during running, while they were suppressed by visual stimuli or when visual flow started while mice were stationary.

Experience-dependent visual plasticity of ChCs and NV-PyCs

The observation that ChCs are suppressed by visual stimulation in the virtual tunnel was unexpected, as our grating (**Fig. 2**) and natural image (**Fig. 3**) experiments showed that ChCs are activated by oriented moving gratings and natural images. However, our passive viewing experiments were performed in mice largely naive to visual stimulation. In contrast, mice behaving in our tunnel paradigm were repeatedly exposed to visual stimulation during the tunnel training phase before we started recording neural activity during behavior. We therefore hypothesized that the observed suppression of ChCs by visual stimulation in the tunnel was caused by experience-dependent plasticity induced by the repeated exposure to visual stimulation during training. To test this, we assessed visual responses in the same neurons to moving oriented gratings before and after training in the virtual tunnel, while mice were passively viewing the stimuli.

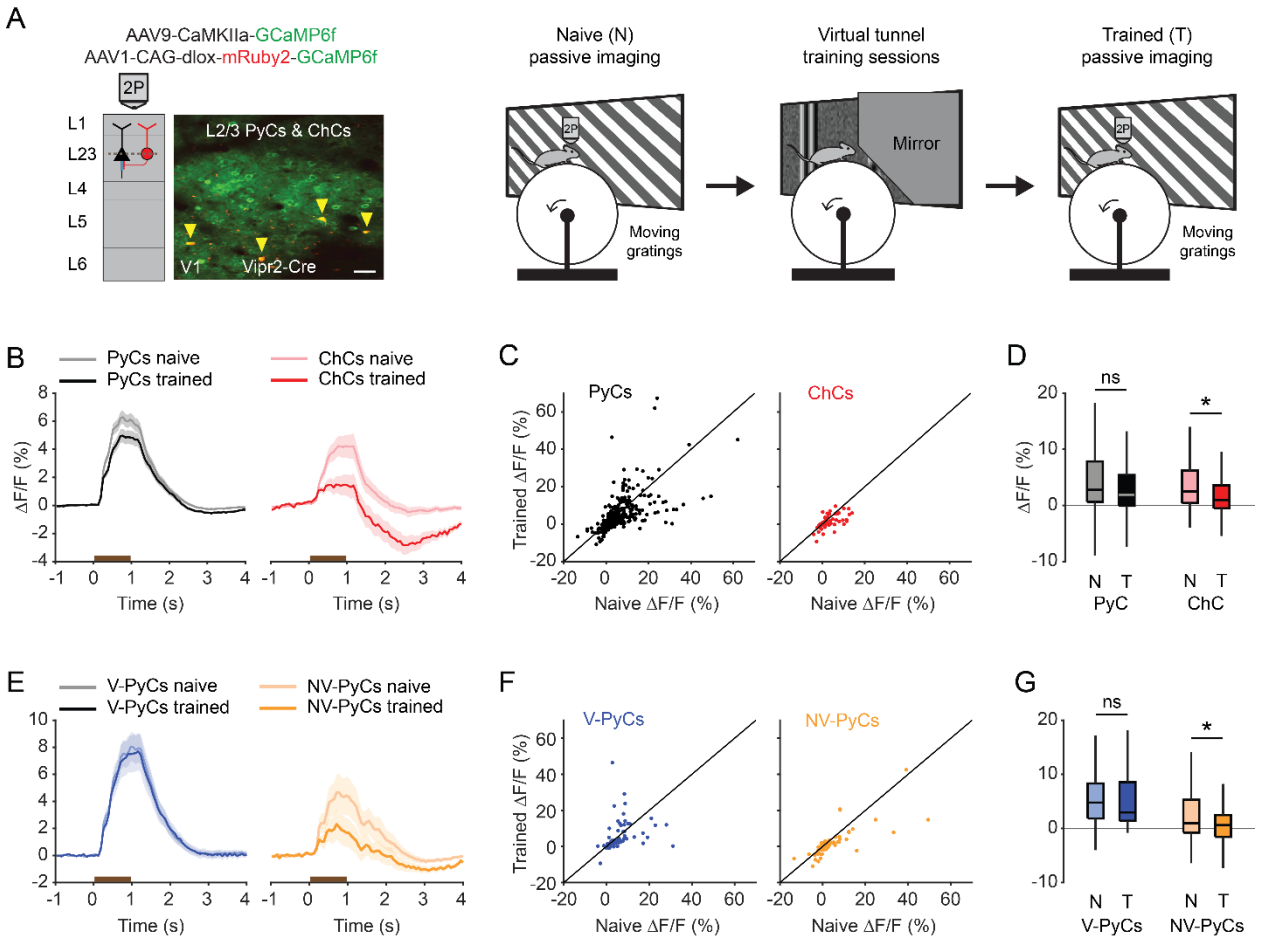

Figure 5. Experience-dependent visual plasticity of ChCs and NV-PyCs

(A) Schematic of viral strategy and experimental setup. In the passive imaging sessions before and after training, mice were imaged while they passively viewed moving gratings. In between those sessions mice were trained in the virtual tunnel where they were repeatedly exposed to visual stimuli. Yellow arrows point to ChCs. Scale bar, 50 µm.

(B) Average population response traces to a 1 s (brown bar) moving grating for all PyCs and ChCs chronically imaged and matched in 'naive' and 'trained' sessions (n = 411 PyCs and 51 ChCs, 8 sessions from 5 mice). Traces represent mean +- SEM over neurons.

(C) Single cell visual response magnitude pre and post training (averaged over 0.2-1.2 s after stimulus onset).

(D) Average visual response magnitude in naive (N) and trained (T) conditions. ChCs, but not PyCs, show plasticity after training. LMEM for all comparisons, *: $p < 0.05$, ns: not significant. Box plots represent median, quantiles and 95% confidence interval (CI) over neurons.

(E) As in B, but for all PyCs chronically imaged and matched in naive, tunnel and trained sessions (n = 68 V-PyCs and 71 NV-PyCs, 5 sessions from 3 mice.

(F) As in C, but for PyC subtypes.

(G) As in D, but for PyC subtypes. NV-PyCs show plasticity after training.

In naive mice, both PyCs and ChCs responded strongly to visual stimulation. Interestingly, the same ChCs showed weak or even suppressed visual responses after mice had been trained in the tunnel (**Fig. 5A-D**). In contrast, the response strength of PyCs was only mildly and non-significantly reduced after training (**Fig. 5D**). OSI and DSI were unchanged after training (PyC OSI: $p = 0.1316$, PyC DSI: $p = 0.9573$, ChC OSI: $p = 0.2199$, ChC DSI: $p = 0.9774$, table S1). These results indicate that ChC responses underwent sensory-evoked plasticity during the repeated visual exposure, even though the visual stimuli were different from those encountered during training in the virtual tunnel. This is in line with our observation that ChCs are weakly selective to visual stimuli.

Visuomotor experience in the virtual tunnel induces plasticity of ChC-AIS connectivity

Previous work has shown that prolonged chemogenetic activation of ChCs or PyCs results in plasticity of ChC bouton numbers at the AIS (*18*). In addition, PyC activation also causes geometric plasticity of the AIS location and/or length (*59–63*). We therefore hypothesized that, in addition to the changes in response properties of ChCs, the visuomotor experience in the virtual tunnel paradigm may induce axonal plasticity of ChCs. To test this hypothesis, we used immunohistochemistry on V1 slices to visualize L2/3 PyC AISs and boutons of tdTomato-labeled ChCs in naive mice and mice after virtual tunnel training (**Fig. 6A**).

We first quantified putative ChC boutons on the AIS of L2/3 PyCs (**Fig. 6A**). While the average number of ChC boutons per AIS remained constant (~2-3 ChC boutons/AIS, **Fig. 6B,C**), we observed that visuomotor experience increased the fraction of AISs being contacted by ChCs (**Fig. 6D**). We also found that the AIS of PyCs in trained mice were shorter than in naive mice (**Fig. 6E-F**), resulting in an increased density of ChC boutons (i.e. ChC boutons per µm AIS length, **Fig. 6G**). Finally, we found that ChC boutons were localized more closely to the base of the AIS (**Fig. 6H-I**).

Taken together, these results show that training in our visuomotor task not only induced plasticity of response properties of ChCs in V1, but also increased the number of AISs with putative ChC contacts and caused activity-dependent AIS shortening of their post-synaptic PyC targets (**Fig. 6J**).

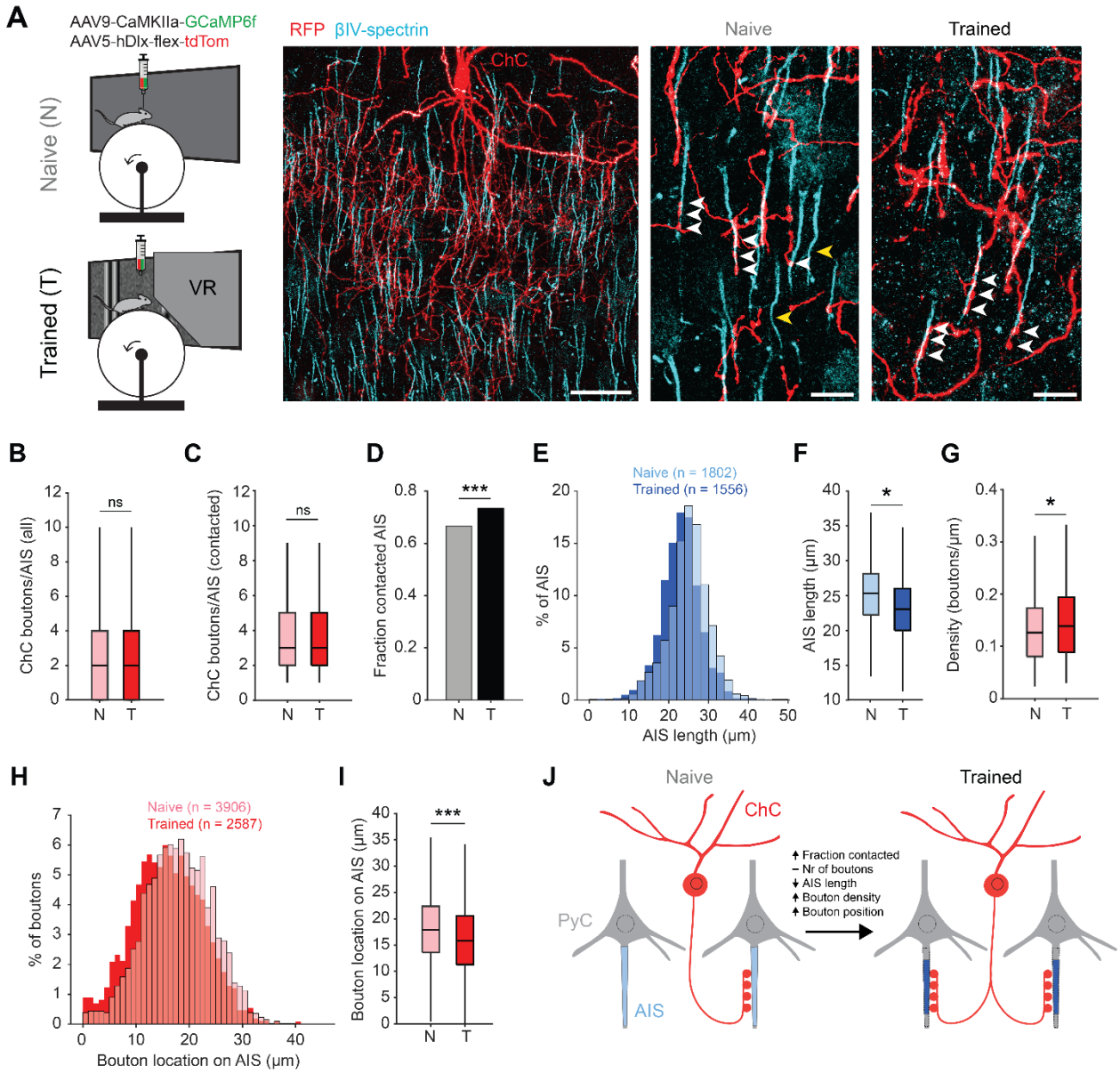

Figure 6. Training in the virtual tunnel induces plasticity of ChC-AIS connectivity

(A) Left: experimental design showing naive mice and mice trained in the virtual tunnel. Middle: confocal image showing V1 L2/3 after immunostaining to visualize ChC processes (α-RFP) and the AIS (α-βIV-spectrin). Scale bar, 30 µm. Right: example colocalization (white) of ChC (red) and AISs (cyan in naive and trained mice. White arrows show putative ChC boutons on AISs. Yellow arrows point to uncontacted AISs. Scale bars, 10 µm.

(B) The average number of boutons on all AISs is similar between naive and trained mice. 5 naive and 3 trained mice, 2-3 slices per mouse, n = 1802 AISs (N) and 1007 AISs (T). LMEM for all comparisons, ***: $p < 0.001$, **: $p < 0.01$, **: $p < 0.05$, ns: not significant. Box plots represent median, quantiles and 95% confidence interval (CI).

(C) The number of boutons on AISs with at least 1 bouton is unaffected by training. 5 naive and 3 trained mice, 2-3 slices per mouse, n = 1200 AIS (N) and 738 AIS (T).

(D) Fraction of cells contacted by at least 1 ChC bouton increases with training. $X^2(1)=13.53$, ***: $p < 0.001$, 5 naive and 3 trained mice, 2-3 slices per mouse, n = 1802 AIS (N) and 1007 AIS (T).

(E) Histogram of AIS lengths in naive and trained mice.

(F) AIS length is decreased by training. 5 naive and 5 trained mice, 2-3 slices per mouse, n = 1802 AISs (N) and 1556 AISs (T).

(G) Bouton density on the AIS is increased by training. 5 naive and 3 trained mice, 2-3 slices per mouse, n = 1200 AIS (N) and 738 AIS (T).

(H) Histogram showing absolute location of boutons on the AIS.

(I) Average bouton location on the AIS. Boutons in trained mice are located more closely to the start of the AIS. 5 naive and 3 trained mice, 2-3 slices per mouse, n = 3906 boutons (N) and 2587 boutons (T).

(J) Schematic model of the changes observed in trained mice vs naive mice.

ChCs weakly inhibit PyC activity independent of locomotion speed

There has been controversy on whether ChCs hyperpolarize or depolarize their postsynaptic PyC targets (*18–23*). However, recent work in adult mice has reported hyperpolarizing and shunting effects in prelimbic cortex, S1 and hippocampus (*18*, *26*, *27*). In order to study postsynaptic effects of ChC activity on L2/3 PyCs in V1 we used inhibitory k-opioid receptor(KORD)-based chemogenetics (*64*) to globally silence ChCs in V1. We expressed KORD-mCyRFP1 or tdTom (control group) in Vipr2-Cre mice along with GCaMP6f (**Fig. 7A**). We then recorded 15 min of ChC and L2/3 PyC activity before and after injection of the KORD ligand Salvinorin B (SalB, 10 mg/kg, s.c.) while mice were allowed to freely run or rest in front of a gray screen. We first looked at the average activity of neurons in both essions. Surprisingly, L2/3 PyCs showed only a mild increase in activity after SalB injection, even though ChC activity was strongly and significantly reduced (**Fig. 7B**).

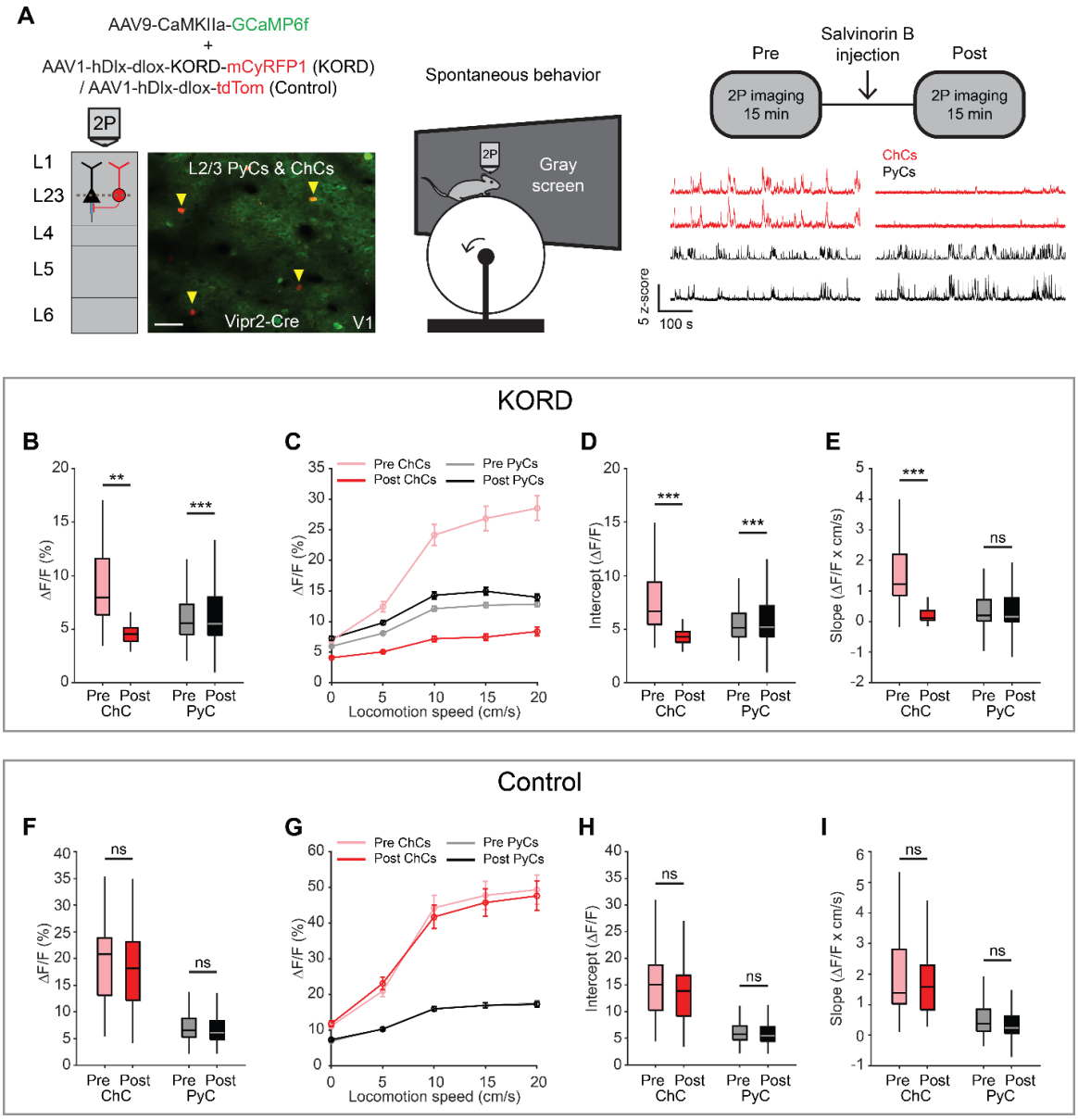

Figure 7. ChCs weakly inhibit PyC activity independent of locomotion speed

(A) Viral strategy and experimental design for chemogenetic silencing of ChCs (yellow arrows) in awake mice. Activity of ChCs and PyCs was recorded before and after an s.c. injection of SalB (10 mg/kg). Bottom right: example traces of two ChCs and two L2/3 PyCs before and after injection of SalB. Scale bar example field of view, 50 µm.

(B-E) Activity and locomotion modulation fit parameters in mice expressing KORD-tdTom in ChCs.

(B) Average ChC activity decreases, while PyC activity increases after injection of SalB. LMEM for all comparisons, ***: $p < 0.001$, **: $p < 0.01$, *: $p<0.05$, ns: not significant (n = 84 ChCs and 1669 PyCs, 12 sessions from 12 mice). Box plots represent median, quantiles and 95% confidence interval (CI) over neurons.

(C) Activity of ChCs and PyCs as a function of locomotion speed before and after injection of SalB.

(D) Average intercept of locomotion modulation fit before and after injection of SalB. The intercept decreases for ChCs but increases for PyCs.

(E) Average slope of locomotion modulation fits before and after injection of SalB. The slope decreases for ChCs but remains unchanged in PyCs.

(F-I) Activity and locomotion modulation fit parameters in mice expressing tdTom in ChCs (Control group).

(F) As in B, but for the control group (n = 37 ChCs and 968 PyCs, 7 sessions from 7 mice).

(G) As in C, but for control group.

(H) As in D, but for the control group.

(I) As in E, but for the control group.

Considering the strong modulation of ChCs by arousal, we next looked at effects of ChC silencing on L2/3 PyC activity across different locomotion speeds. Binning activity based on locomotion speed again revealed the relationship between locomotion and ChC activity and to a lesser extent L2/3 PyC activity (**Fig. 7C**). Although the locomotion modulation curve of ChCs decreased in both amplitude and steepness after SalB injection, only the amplitude was affected for PyCs. Indeed, a linear fit of activity as a function of locomotion speed before and after SalB injection confirmed that the intercept but not the slope of the fit was increased for PyCs (**Fig. 7D-E**). We found no differences in the control group (**Fig. 7F-I**). In addition, to test whether the effect of silencing ChCs preferentially affected PyCs that were weakly or strongly modulated by locomotion, we correlated the locomotion modulation index (LMI) for each PyC with the change in $\Delta F/F$ due to ChC silencing (after minus before). The correlation was weak and not significant ($r = 0.0068$, $p = 0.7827$), showing that ChCs do not differentially target PyCs based on locomotion modulation. In contrast to the idea that ChCs exert powerful control over action potential generation, these results suggest that ChCs only weakly modulate PyC activity, independently of locomotion speed.

Discussion

In this study we investigated the connectivity and function of chandelier cells (ChCs) in V1. We find that ChCs receive input from local L5 PyCs and higher-order cortical regions and show strong arousal-related activity. While they are also visually responsive, ChCs are weakly selective for stimulus content. Furthermore, we found that visuomotor experience in a virtual tunnel paradigm induces plasticity of the visual responses of ChCs as well as their axo-axonic synapses at L2/3 PyC AISs.

Recent EM reconstructions have shown that although most L2/3 PyCs in V1 receive ChC input, the number of ChC boutons on the AISs of PyCs varies significantly and correlates with their size and laminar depth (*13*). Accordingly, we found that ChCs provided GABAergic inputs to many of the L2/3 PyCs in their vicinity. Unexpectedly, our

retrograde rabies virus tracing experiments showed that ChCs receive most of their input from local L5 PyCs. In keeping with the identified circuits, we did not detect L2/3 PyCs providing inputs to ChCs using dual patch clamp recordings, suggesting that the rabies labeled neurons in layers 1-4 were predominantly interneurons, in line with previous work (*40*). ChCs also received long-range inputs from various thalamic and cortical regions (e.g., dLGN, LP, RSC, S1), matching those innervating other interneuron subsets in V1 (*36*). Optogenetic activation of cortical feedback induced responses in almost all V1 ChCs and repeated stimulation caused synaptic depression, indicating a high release probability, which is usually seen in strong cortical inputs to V1 interneurons (*36*). Taken together, the connectivity pattern of ChCs in V1 thus appears to be non-reciprocal, as is also observed in prelimbic cortex (*26*). However, in contrast to prelimbic cortex where ChCs receive input from deep layer 3 PyCs, we show here that V1 ChCs receive most of their input from layer 5.

Although ChCs in V1 are sparse and the number of starter ChCs in our rabies tracing experiments was relatively low, we found large numbers of L5 PyCs providing monosynaptic input to them. This means that each ChC receives input from many L5 PyCs, which could explain the low selectivity of ChC responses we observed to natural images compared to those of L2/3 and L5 PyCs. This is also supported by the MEIs we obtained from the pre-trained CNN. MEIs of L5 PyCs were often high-contrast oriented patterns, like those of L2/3 PyCs, or more complex textures. Instead, MEIs of ChCs were of lower contrast and less structured and similar to MEIs created to maximally drive large numbers of L5 PyCs. Combined inputs from L5 PyCs with diverse tuning properties are also expected to result in tuning to low spatial frequencies, large RFs and low orientation tuning, matching the modelled ChCs. Finally, modelled ChCs also displayed weak contrast tuning. This is an expected consequence of the preference for low spatial frequencies, as these require lower contrast to be detected (*50*, *51*).

In our virtual tunnel paradigm, ChCs were active during locomotion but even more so during visuomotor mismatch caused by halting the tunnel while the mice were running. Surprisingly, ChC activity was suppressed by the visual stimuli in the tunnel, or when the visual flow started while the mice were stationary. We found that this apparent discrepancy with the strong responses to natural stimuli could be explained by experience-dependent plasticity of ChC activity: while ChCs responded vigorously to oriented-bar stimuli in naive mice, these responses were almost absent after training in the virtual tunnel. This experience-dependent plasticity of ChC responses has not been described before. While the underlying mechanisms remain to be investigated, there are several possibilities. First, it could be caused by reduced excitatory synaptic transmission of visual input to ChCs or increased visually driven inhibition. Second, the plasticity could involve changes in the response properties of L5 PyCs providing input to ChCs. Interestingly, recent evidence shows that during visuomotor behavior, intratelencephalic (IT) L5 PyCs respond in a similar fashion as ChCs in that they respond to running and visuomotor mismatch but are suppressed by unexpected visual flow (*65*). Whether L5 IT PyCs are the main L5 PyC subset providing input to ChCs remains to be investigated. A third option is that the experience-dependent changes in ChC activity are related to arousal. ChCs were previously shown to display arousal-related activity in various brain regions (*13*, *27*, *29–31*), which matches our observation that their activity is highly correlated with running and pupil size. In addition, the neuromodulator acetylcholine (ACh) is involved in axonal arborization of developing ChCs, further underlining the relationship

between ChCs and arousal (*66*). During training in the virtual tunnel, mice become acquainted with visual stimuli and learn that running consistently results in visual flow. After training, visual stimuli may thus cause less arousal while unexpected visual flow halt during running may cause more. In line with this idea, it was recently shown that visuomotor mismatch induces strong noradrenergic input to V1 (*56*). Noradrenergic input has been shown to depolarize ChCs in frontal cortex (*67*). However, we did not identify neuromodulatory inputs to ChCs in our rabies tracing experiment. Possibly, these inputs act predominantly through extrasynaptic receptors and were therefore not labeled by the transsynaptic rabies approach. Future experiments may reveal to what extent plasticity of ChC responses is stimulus specific or arousal related.

When examining how neurons respond to expected or unexpected visual input, it is useful to consider the concept of predictive coding (*68–75*). In this framework, an internal representation of the world is compared with sensory inputs and updated based on prediction errors: the differences between the expected and actual sensory inputs. These prediction errors can be negative, signaling the absence of an expected visual stimulus, or positive, signaling the presence of an unexpected visual stimulus. It has been suggested that prediction errors may be computed by L2/3 PyCs, while the internal representation is encoded by local L5 PyCs and top-down inputs from higher order brain regions (*65*, *74*, *76*). Previous work has shown that in V1, L2/3 PyCs indeed respond to mismatches between visual flow and locomotion (*7*, *53–55*). Recent evidence suggests that two genetically defined subpopulations of L2/3 PyCs preferentially respond to (unexpected) visual stimuli, which could be considered positive prediction errors, or visuomotor mismatch, which could be seen as negative prediction errors (*52*). In line with these findings, we observed two functional clusters of PyCs in L2/3, one responding predominantly to visual stimuli (V-PyCs) and the other to visuomotor mismatch (NV-PyCs).

Prediction error responses require inhibitory neurons to compute the difference between expectation and actual visual input. As ChCs receive input from L5 and higher order cortical regions, they might contribute to calculating positive prediction errors by subtracting the internal representation (i.e. the predicted stimulus) from the actual visual input. However, as ChCs only mildly inhibited L2/3 PyCs, they may not be well suited for this function. Moreover, given that ChCs are highly correlated in their activity, it seems unlikely that they contain high dimensional prediction error information. Predictive coding also involves updating of the internal representation based on prediction errors. Recent evidence suggests that this plasticity requires a gating signal that is provided by noradrenergic input (*56*). One option is therefore that ChCs also encode arousal and play a role in the regulation of plasticity.

An intriguing possible mechanism through which ChCs could regulate plasticity is by controlling geometric modifications of the AIS of L2/3 PyCs. We found that visuomotor experience in the virtual tunnel resulted in AIS shortening and more AISs with putative ChC contacts. This is in agreement with previous work showing that chemogenetically activating L2/3 PyCs results in increased innervation by ChCs and decreased AIS length (*18*). AIS shortening is known to reduce PyC excitability (*60*) and likely represents a homeostatic plasticity mechanism. It has been suggested that increased ChC innervation also contributes to homeostatic control by reducing action potential

generation (*18*). Considering our observation that *in vivo* chemogenetic silencing of ChCs only mildly increased L2/3 PyC activity, their electrical contribution to vetoing action potential output seems, if anything, limited. These findings are thus in contrast with the general notion that ChCs exert powerful control over PyC output (*28*, *77*), but consistent with computational simulations predicting a relatively small inhibitory effect of GABAergic innervation of the AIS, possibly involving shunting inhibition (*78*, *79*). Interestingly, ChC boutons face postsynaptic sites where cisternal organelles are located with micrometer precision (*13*, *80*). As cisternal organelles are implicated in calcium signaling and AIS plasticity (*81*), ChCs may thus effectively influence these events. In this scenario, ChC activation could prevent homeostatic AIS shortening of L2/3 PyCs if their activity occurs during behaviorally relevant, arousal inducing events. Testing this hypothesis would require, for example, studying the consequences of synchronous or asynchronous activation of ChCs and PyCs on AIS plasticity. The emerging availability of mouse models to genetically target ChCs (*13*, *14*, *26*, *27*, *33*) and novel live markers of the AIS (*82*) are making such experiments possible.

In conclusion, our comprehensive study of the function and connectivity of ChCs in V1 reveals that ChC activity is primarily driven by arousal-inducing events such as unexpected visual stimuli, visuomotor mismatch and locomotion. We also observed remarkable plasticity of ChC responses by visuomotor experience, as well as in their innervation of the AIS. Interestingly, our results indicate that *in vivo*, ChCs do not exert strong control over action potential generation at the AIS, but only provide a weak inhibitory influence on PyC activity. Future experiments may reveal whether ChCs provide a gating signal for AIS plasticity and elucidate the underlying mechanisms.

Materials and Methods

Mice

All experiments were approved by the institutional animal care and use committee of the Royal Netherlands Academy of Arts and Sciences. We used both male and female mice for all experiments. For a subset of tunnel experiments, we used Vipr2-Cre mice crossed with Pvalb-T2A-FlpO-D and AI65(RCFL-tdT)-D (Jackson Laboratories, www.jaxmice.jax.org, strain 031332, 022730 and 021875, respectively (*13*, *33*)). For experiments with natural images (Fig. 3), we used Vipr2-Cre mice crossed with CBA/JRj (Janvier labs) mice for targeting ChCs and L2/3 PyCs and Rbp4-Cre mice (line KL100, GENSAT project) for targeting L5 PyCs. We used Vipr2-Cre mice for all other experiments. Mice were group housed under a 12 h reversed day/night cycle and provided with *ad libitum* access to food and water. Experiments were performed in the dark phase. Mice had access to a running wheel in their home cage throughout the duration of the experiment.

Viral injections & window surgery

For all cranial surgical procedures, mice were anesthetized with isoflurane (4% induction, 1.6% maintenance in oxygen). During the surgeries, temperature was maintained at 37 degrees with euthermic pads and eyes were protected from light and drying using Cavasan eye ointment. For viral injections targeting L2/3 in all experiments except those used for CNN modeling, the skull was exposed, three small craniotomies were drilled in the skull overlying right V1 (centered around 2.9 mm lateral, 0.5 mm anterior to lambda), and one injection of 70-120 nl virus

(titer ~10E12 viral genomes per mL) in each craniotomy at a depth of approximately 250 µm was made. We used one or more of the following viruses as indicated in the figures: AAV9-CaMKIIa-GcaMP6f, AAV1-CAG-flex-mRuby2-GcaMP6f, AAV1-hSyn1-GcaMP6f, AAV-PHP.eB-shortCAG-dlox-GcaMP6f(rev)-dlox, AAV5-hDlx-DIO-eYFP-t2A-TVA, AAV9-hDlx-DIO-oG, Rbv-ΔG-mCherry, AAV1-hDlx-dlox-hKORD-mCyRFP1(rev)-dlox, AAV1-hDlx-dlox-ChrimsonR-tdTomato(rev)-dlox, AAV9-CaMKIIa-ChR2-eYFP (also see key resource table). For L2/3 CNN model experiments (Fig. 3) we drilled 7 holes across the visual cortex (centered around 2.9 mm lateral, 0.5 mm anterior to lambda) and injected 70-120 nl virus (AAV9-CaMKIIa-GcaMP6f and AAV1-hDlx-dlox-mCyRFP1(rev)-dlox, titer ~0.7*10E12 viral genomes per mL) across two depths (200 and 400 µm). For L5 CNN model experiments (Fig. 3), we performed i.v. injections in the tail vein of awake body-restrained mice using 125 µl virus (AAV-PHP.eB-shortCAG-dlox-GcaMP6f(rev)-dlox, titer ~3.4x10E12 viral genomes per mL). All mice were allowed to recover from viral injections for two weeks.

For the cranial window surgery, mice were implanted with a double (3+4 mm diameter) or triple (4+4+5 mm diameter, for L2/3 CNN experiments) glass window on the center of V1. To allow head-fixation, mice were implanted with a custom metal head-ring (5 mm inner diameter). The glass window and head-ring were fixed to the skull using dental cement. At least one week after surgery, mice were handled and habituated to being head immobilized in our setup until they sat comfortably and started running regularly on their own (typically ~5 sessions).

Visual stimuli and virtual tunnel

All visual stimuli for two-photon imaging were presented on a gamma-corrected full HD LED monitor using OpenGL and Psychophysics Toolbox 3 running on MATLAB (Mathworks). The monitor was positioned 15 cm from the mouse. For passive visual stimulation before and after training, we used full screen square gratings (0.05 cpd) of different contrasts (0-0.05-0.1-0.2-0.4-0.8-1) moving in one of eight different directions (45° apart, 1 cps). Stimuli were presented for 1 s with a random inter trial interval of 4-6 s and repeated a minimum of eight times each.

To model visual RF selectivity using the CNN model, we used 3600 unique images from 720 classes taken from the THINGS database (*83*). In order to test reliability across repetitions of the same stimuli and model cross-validated correlations, an additional 40 unique images were repeated 10 times. Individual images were composed of two square images from the same category, blended to cover the whole screen. Images were shown for 0.5 s, followed by a delay of 0.5 s where mice viewed a gray screen. CNN experiments were performed on naive mice.

For our virtual reality setup, we measured absolute running speed via a rotary encoder, which enabled real-time rendering of the virtual corridor. The left half of the corridor was displayed on a monitor positioned at a 45° angle and viewed through a mirror, giving the perception of a symmetrical tunnel. The virtual environment was created using Psychophysics Toolbox 3 and OpenGL running on MATLAB. The corridor was 100 cm long and its walls were covered in a black and white Gaussian noise texture, with visual stimuli superimposed. This included three vertical

gratings and three checkerboard stimuli placed 11 cm apart between the distances of 22-77 cm (Fig. 4B). Following a run through the visual part of the corridor, mice were exposed to a luminance-matched gray screen, followed by an 8 kHz auditory cue after 1 s, and then received a 5 µl water reward 2 s later. Mice were trained over a minimum of six sessions, with one session per day, until they consistently completed over 70 trials. Mice continued to be trained in between imaging sessions until the experiment was completed. For open loop experiments, visual flow speed was set at a constant 20 cm/s. Visuomotor mismatches were only introduced during the experimental sessions and were achieved by briefly halting the visual flow for 0.5 s at random locations in the visual section of the tunnel where visual stimuli appeared (between 20-80 cm). Mismatches were restricted to periods where the mouse was running during closed loop sessions and periods where the mouse was stationary during open loop sessions.

Two-photon calcium imaging

Data collection

Two-photon imaging experiments were performed on a two-photon microscope (Neurolabware) equipped with a Ti-sapphire laser (Mai-Tai 'Deepsee', Spectraphysics; wavelength, 920 nm) and a 16x, 0.8 NA water immersion objective (Nikon) at a zoom of 1.6x for L2/3 imaging and a zoom of 2x for L5 imaging. The microscope was controlled by Scanbox (Neurolabware) running on MATLAB. Images were acquired at a frame rate of 15.5 or 31 Hz. In some sessions, we performed dual-plane imaging at 31 Hz using an electrically tunable lens (OptoTune), resulting in an effective frame rate of 15.5 Hz per plane. For L2/3 experiments, somatic imaging was performed at ~150-300 µm depth. For L5 experiments, we recorded apical dendrites at a depth of ~200 µm. Pupil size and position was tracked at the imaging frame rate using an IR camera (Dalsa Genie).

Preprocessing

We used the SpecSeg toolbox for preprocessing as described in detail before (*84*). In short, we performed rigid motion correction using NoRMCorre (*85*) followed by automated region-of-interest (ROI) selection based on cross-spectral power across pixels. After manual refinement, raw ROI signals were extracted and corrected for neuropil by subtracting the average pixel values in an area surrounding each ROI multiplied by 0.7. ΔF/F traces were made by subtracting a moving baseline (10th percentile over 5000 frame windows) and dividing by a linear fit over that baseline. Matching of chronically recorded neurons was performed using the chronic matching module of SpecSeg.

Passive sessions

For comparing single-cell responses between conditions we first matched neurons that we chronically imaged across multiple sessions. For subsequent analyses we only selected neurons that we found back in all sessions relevant for that analysis (e.g., pre-post or pre-tunnel-post). For statistical analyses, we took the mean ΔF/F trace over all stimuli and computed the baseline-corrected average from 0.2 to 1.2 s after stimulus onset for each cell. We removed all trials in which the running speed exceeded 1 cm/s anywhere from 1 s before until 4 s after stimulus onset.

To correlate activity with estimates of arousal, mice were allowed to freely run or rest in front of a gray monitor for ~10 min. We computed the correlation coefficient between calcium activity of each cell with running speed and

pupil size using the 'corr' function in MATLAB. For pairwise correlations between neurons within each cell type, we computed the average correlation coefficient during stationary periods (running speed < 1 cm/s) for each cell with all other cells of that type within the field of view. For displaying purposes (Fig. 2B), we z-scored single cell traces over the entire 10 min session.

For orientation- and direction tuning we took the baseline-corrected average from 0.2 to 1.2 s after stimulus onset for each cell. For tuning and response strength calculations in Fig. 2 and Fig. 5 we only included contrasts higher than 0.7. For orientation tuning, the mean responses to the eight orientations (θ) were fit with a single circular Gaussian using nonlinear least-squares fitting as follows:

$$R(\theta) = C + R_p \mathrm{e}^{\frac{-ang_{ori}(\theta-\theta_{pref})^2}{2\sigma^2}}$$

where R(θ) is the response to the grating of orientation θ, C is an offset term, Rp is the response to the preferred orientation, ang_{ori}(x)=min[abs(x), abs(x -180),abs(x +180)] wraps angular differences to the interval 0° to 90°,and σ is the standard deviation of the Gaussian. For direction tuning, the mean responses to the eight directions (θ) were fit with a double circular Gaussian:

$$R(\theta) = C + R_p \mathrm{e}^{\frac{-ang_{ori}(\theta-\theta_{pref})^2}{2\sigma^2}} + R_n \mathrm{e}^{\frac{-ang_{ori}(180+\theta-\theta_{pref})^2}{2\sigma^2}}$$

where R_p is the fitted response at the preferred direction, R_n is the fitted response at the non-preferred direction, ang_{dir}(x)=min[abs(x), abs(x-360),abs(x +360)] wraps angular differences to the interval 0° to 180°

Orientation tuning strength was calculated using 1-CircVar:

$$1- \ CircVar = \left|\frac{\sum_k R(\theta_k)e^{2i\theta_k}}{\sum_k abs[R(\theta_k)]}\right|$$

where $R(\theta_k)$ is the response to the orientation θ_k (in radians). Direction tuning strength was also assessed using 1-CircVar using the following equation for directional data:

$$1- \ CircVar = \left|\frac{\sum_k R(\theta_k)e^{i\theta_k}}{\sum_k abs[R(\theta_k)]}\right|$$

where θ_k is the direction of the grating (in radians). Orientation and direction tuning responses were normalized to their maximum response before calculating 1-CircVar. Orientation and direction tuning curves used for plotting

were computed by shifting the average tuning curve to the cell's fitted preferred direction, followed by averaging across cells to compute cell type averages.

CNN model

As input to our CNN model we used spike probabilities generated using CASCADE (*86*) from neuronal responses to 2600 natural images. We took the single-cell average spike probability between 0 and 0.5 s after stimulus onset as the response to each natural image. To model the neuronal responses we employed a pre-trained CNN (*87*) ("Inception v1") and fit a mapping function to the activations of a target layer (*44*). In brief, for each neuron we learned a set of 2D spatial weights (W_s) with size equal to the size of a channel of the target CNN layer (i.e. the pixels) and a set of feature weights (W_f) with size equal to the number of channels of the target CNN layer. The W_s learned the spatial RF of each neuron, while the W_f learned their feature selectivity as a weighted sum over the features of the pre-trained CNN layer. Thus, the predicted response of a neuron n (i.e., $\widehat{y_n}$) was computed according to:

$$\widehat{y_n} = \left[\sum W_s^{(n)} * X_l\right] * W_f^{(n)}$$

Where X_l are the batch-normalized activations from the target CNN layer l. The weights were jointly optimized across all neurons to minimize the prediction error $\mathcal{L}_{error}$ regularized by a combination of a smoothing Laplacian loss ($\mathcal{L}_{Laplace}$: see below) over W_s (*44*), to encourage smooth spatial RFs, a L1 loss ($\mathcal{L}_1$: see below) over W_f to encourage sparsity/selectivity of the features (*42*, *43*) and a L2 loss ($\mathcal{L}_2$: see below) over both parameters (*43*, *44*). Thus the cost function was computed as follows:

$$\mathcal{L}_{error} = \sqrt{\sum_n (\widehat{y_n} - y_n)^2}$$

$$\mathcal{L}_{Laplace} = \lambda_s \sqrt{\sum_n (W_s^{(n)} * L)^2}, L = \begin{bmatrix} 0 & -1 & 0 \\ -1 & 4 & -1 \\ 0 & -1 & 0 \end{bmatrix}$$

$$\mathcal{L}_1 = \lambda_f \sum_n \left|W_f^{(n)}\right|$$

$$\mathcal{L}_2 = \lambda_2 \sum_n (W_s^{(n)^2} + W_f^{(n)^2})$$

$$\mathcal{L} = \mathcal{L}_{error} + \mathcal{L}_{Laplace} + \mathcal{L}_1 + \mathcal{L}_2$$

Where y_n is the response of neuron n. The hyper-parameters (l, λ_s, λ_f, λ_2 and the learning rate) were selected using a grid search and then selecting the combination yielding the highest correlation in the training set. For all cell

types, the best target CNN layer (l) was "*conv2d2*". The model was implemented in PyTorch (*88*) and optimized with Adam (*89*) in 600 epochs with a batch size of 128 and early stopping (every 200 epochs, decay factor = 3).

After training, we generated the MEIs by optimizing the pixels in the input to maximize the response of each model neuron independently. To ensure the stability and interpretability of the MEIs, we introduced preconditioning and regularizations to avoid high-frequency artifacts (*90*), and specifically frequency penalization and transformations (padding, jittering, rotation and scaling). Optimization of the MEIs was done using Lucent (i.e. PyTorch implementation of Lucid (*90*)) with Adam (learning rate = 1e-2, weight decay = 1e-3) in 50 epochs. To generate MEIs for combinations of L5 PyCs (**Fig. S2F**), we first randomly chose 10 starter L5 PyCs. On each iteration we then added 5 random L5 PyCs (except for the first iteration, where we added 4) and optimized a 'composite MEI' by maximizing the summed responses from all neurons.

Furthermore, for each neuron we computed a few metrics either directly on the data or by analyzing model responses to novel stimuli. The response strength of each neuron was computed by taking the maximum response of the time-course averaged over all images, divided by the standard deviation of the response in the 200 ms before the stimulus onset. In addition to the 3,600 images used for training, we also recorded responses to 40 images that were presented 10 times each (4,000 images in total) to test the generalization performance of the model. We computed the selectivity to visual input as the sparsity of their response distribution (*49*), going from 0 (not sparse) to 1 (maximally sparse) as follows:

$$\text{Sparsity } = [1 - \frac{\sum(R_i/40)^2}{(\sum R_i^2/40)}] \Big/ [1 - (\frac{1}{40})]$$

Where R_i is the response to i^{th} image and 40 is the number of test images.

For population decoding, we performed LDA using the 'fitcdiscr' function in Matlab on the neuronal responses to the 40 test images. For each decoding run, we trained an LDA decoder by randomly selecting 80% of the trials and then testing the decoder on the remaining 20% of trials. We repeated this procedure 50 times to account for variability between trials. For ChCs, we used the total population (n = 34) and averaged the resulting 50 decoding accuracies. For L2/3 PyCs, we performed 1000 iterations of 50 runs each by randomly subsampling 34 neurons on each iteration. For each iteration we then averaged the 50 runs, resulting in a distribution of 1000 decoding accuracies. Statistical significance was determined using a permutation test of the average ChC decoding accuracy (12.55%) versus the distribution of 1000 L2/3 PyC accuracies. Chance level decoding was at 2.5% (40 images total).

We also computed the oracle correlation of each neuron by correlating the responses to multiple repetitions of the same 40 test images and then taking the average correlation (*43*). Only neurons with an oracle correlation higher than zero were included in the model. In order to test the performance of the model we correlated the predicted responses with the recorded neuronal responses to the 40 test images (not used for training). The resulting 'cross-validation correlations' were largely identical to the oracle correlations for all cell types (**Fig. S2B-C**).

We computed the RF size as the full width at half maximum of a 2D Gaussian fitted to W_s of each neuron. Neurons with RF size > 40 degrees were excluded from analysis.

We determined the orientation tuning by showing to the model neurons full-contrast Gabor gratings with 8 different orientations (22.5 degrees apart), 5 spatial frequencies (from 0.02 to 0.08 cycles per degree) and 2 phases (0 and 90 degrees). The orientation selectivity index (OSI) was computed using 1-CircVar as above.

For SF tuning we used 12 SFs (0.01, 0.02, 0.03, 0.04, 0.05, 0.06, 0.08, 0.1, 0.2, 0.3, 0.4, 0.6). The preferred SF was defined as the SF at which the max response for each neuron occurred.

We measured contrast sensitivity using full screen gratings of increasing contrast (0.05, 0.1, 0.2, 0.4, 0.6, 0.8, 1) followed by calculating a linear fit across the contrast tuning responses. We took the slope of the fit as the contrast sensitivity for each neuron.

For pairwise correlations of spike probabilities between neurons within each cell type, we computed the average correlation coefficient during stationary periods (running speed < 1 cm/s) for each cell with all other cells of that type within the field of view.

Virtual tunnel

For the analysis of tunnel data, we removed trials that took longer than 15 s from start until reward delivery. To compute activity as a function of location in the tunnel (0-100 cm) we divided the tunnel into 50 bins of 2 cm each and averaged activity of all frames occurring in a bin, followed by averaging over trials for each cell. Activity for each cell in the non-visual part of the tunnel was time-locked to exit from the visual part until 9 s later and subsequently averaged over trials. For this analysis we removed all trials containing visuomotor mismatch events. Locomotion traces were made by averaging locomotion speed across all trials for each session, followed by averaging normalized traces (between 0 and 1) over mice. For single-cell average activity in the visual part of the tunnel we took the mean activity between 20-80 cm and subtracted the mean activity between 0-20 cm. For the non-visual part, we averaged the entire trace for each cell.

For clustering, we z-scored trial-averaged traces in the visual section of the tunnel from all PyCs as input for the 'linkage' function in MATLAB with 'ward' as method. We then performed clustering using the 'cluster' function with the optimal number of clusters as determined by silhouette evaluation of the traces. Since the result of silhouette evaluation could not exclude the possibility that only 1 cluster was optimal, we tested the separability of the V-PyCs and NV-PyCs clusters using a permutation test. In order to do this, we first computed an average trace combined for the visual and non-visual section for each cell. We then z-scored this trace, and computed the visual response by averaging the z-scored values between 20-80 cm in the visual section of the tunnel. This procedure therefore gave us a single visual responsiveness value for each cell. Next, we binned this distribution of visual responsiveness over

neurons into *n* bins, and normalized the sum of all counts to 1, such that *P* and *Q* describe the discretized probability mass functions for the V-PyCs and NV-PyCs respectively. We then calculated the separability in visual responsiveness between the V-PyCs and NV-PyCs clusters using the Bhattacharyya distance (BD):

$$BD = -\ln\left(\sum_{i=1}^{n} \sqrt{P_i Q_i}\right)$$

Here, P_i and Q_i are the frequencies of samples in 'visual response' bin *i*. The real data we observed gave a BD of 0.4262. Finally, we quantified whether this separability value was higher than could be expected by chance, and therefore whether the V-PyCs and NV-PyCs groups indeed represented distinct clusters. To this end, we generated a distribution of 1000 randomized BD values obtained by shuffling the visual and non-visual responses of all cells, and repeating the procedure as described above. Statistical significance was determined using a permutation test of 0.4262 versus the distribution of 1000 shuffle-randomized populations.

We calculated mismatch responses after correcting for location of the mismatch events, as spatial location in the tunnel can modulate activity of V1 cells even when visual input is identical(*91*, *92*). First, we averaged activity across mismatch trials for each cell. For each mismatch event we then randomly subsampled from control trials (without mismatch events) at identical locations in the tunnel. We repeated this 100 times and subtracted the average trace over repetitions from the real mismatch trace before baseline-correcting for each neuron. Mismatch amplitude was calculated by taking the average of the corrected trace between 0.2 and 1.2 s after mismatch onset. We z-scored each neuron's visual, non-visual and visuomotor mismatch trace for display purposes only (Fig 4C).

Locomotion onset traces were based on running onsets in the non-visual part of the tunnel. Onsets were defined as the first frame in the non-visual section (and after reward delivery) where the average running speed was less than 5 cm/s in a 0.5 s interval preceding the frame, and more than 5 cm/s in the 2 s following the frame. Responses were defined as the baseline-corrected average between 0 and 2 s after onset.

Closed loop visual flow onset traces were made by time-locking (rather than distance) each trial to the start of the visual section. Responses were quantified as the baseline-corrected average between 0.5 and 2 s after trial onset, as the first 20 cm of the tunnel contained no visual stimuli. Only trials that took less than 10 s in the visual section were included in this analysis.

During open loop sessions, the running speed of the mice was uncoupled from visual flow speed, which was fixed at 20 cm/s and followed the regular trial structure. Open loop visual flow onsets were defined as the start of the visual section in trials where the mouse was stationary throughout the visual section. Open loop VF halts were defined as 0.5 s pauses in the VF during stationary trials in open loop condition. For comparison of closed loop mismatch with open loop VF halt we only included trials in closed loop condition during which locomotion speed at mismatch onset was between 5 and 30 cm/s such that the average onset speed was similar as during open loop VF halts (20 cm/s).

Correlations of ChC activity with V-PyCs and NV-PyCs were performed by computing a correlation coefficient on the average ΔF/F trace of the visual and non-visual section combined between pairs of cells. For each ChC, we then averaged the correlation coefficients of that ChC with all V-PyCs or NV-PyCs in that session.

Chemogenetic experiments

For passive chemogenetic experiments we used naïve mice injected with AAV9-CaMKIIa-GCaMP6f along with the inhibitory DREADD AAV1-hDlx-dlox-KORD-mCyRFP1 (KORD group) or AAV1-hDlx-dlox-ChrimsonR-tdTomato (Control group). We recorded activity of PyCs and ChCs for 15 min under gray screen conditions, after which mice were injected with SalB (10 mg/kg in saline, s.c.). Five minutes later, we again recorded activity for 15 minutes. Mice were allowed to run or rest freely. For the analysis of overall activity before and after injection of SalB, we calculated the average ΔF/F of all frames in both recordings for each cell, before averaging over cells for each type. Locomotion modulation curves were computed for each cell by averaging activity over all frames during which the mouse was running at defined speeds within a range. The first bin contained frames during which the mouse was fully stationary (speed = 0 cm/s). All subsequent bins contained frames during which the running speed was between that bin and the previous bin (i.e., bin '10' contained speeds 5-10 cm/s). Speeds >20 cm/s were not included in the analysis as several mice did not reach those speeds in either of the sessions. To get the final population curves we averaged over cells for each type. We computed a linear fit over all samples of activity and running speeds for each cell and session and took the coefficients estimates as the intercept and slope. We then averaged over cells for each type. The locomotion modulation index (LMI) was calculated for each cell as follows:

$$LMI = \frac{\Delta F/F_{run} - \Delta F/F_{stat}}{\Delta F/F_{run} + \Delta F/F_{stat}}$$

Where $\Delta F/F_{run}$ is the average activity during frames when the mouse was running (>1 cm/s) and $\Delta F/F_{stat}$ is the average activity during frames when the mouse was not running (<1 cm/s). We then computed a correlation coefficient between the LMI and the difference in ΔF/F due to ChC silencing.

In vitro electrophysiology

At ~3 months of age, mice were sacrificed for preparation of acute brain slices containing V1. Mice were deeply anesthetized by application of pentobarbital s.p. (60 mg/kg bodyweight). They were perfused with oxygenated N-methyl-D-glucamine containining articificial cerebrospinal fluid (NMDG-ACSF) containing (in mM); 92 NMDG, 30 $NaHCO_3$, 1.25 NaH_2PO_4, 2.5 KCl, 20 HEPES, 25 Glucose, 0.5 $CaCl_2$, 10 $MgCl_2$ (saturated with 95% O_2 and 5% CO_2, pH 7.4) and subsequently decapitated. The brain was swiftly removed and submerged in NMDG-ACSF (composition see above). 300 µm thick coronal slices were cut using a Leica VT 1200S vibratome (Leica Biosystems, Wetzlar Germany). Slices were allowed to recover for 15 min. at 35 °C in NMDG-ACSF. They were subsequently transferred to a holding chamber and kept at room temperature in holding ACSF containing (in mM) 125 NaCl, 25 $NaHCO_3$, 1.25 NaH_2PO_4, 3 KCl, 25 Glucose, 1 $CaCl_2$, 6 $MgCl_2$, and 1 kynurenic acid (saturated with 95% O_2 and 5% CO_2, pH 7.4) until

recordings began. Recordings were carried out at ~32 °C. Slices were transferred to an upright microscope (BX61WI, Olympus Nederland BV) and constantly perfused with oxygenated ACSF containing (in mM) 125 NaCl, 25 $NaHCO_3$, 1.25 NaH_2PO_4, 3 KCl, 25 mM Glucose, 2 $CaCl_2$ and 1 $MgCl_2$. The chamber was perfused at a rate of 3 ml/min. Cells were visualized with a 40x water immersion objective (Achroplan, NA 0.8, IR 40x/0.80 W, Carl Zeiss Microscopy) with infrared optics and oblique contrast illumination. Patch pipettes were pulled from borosilicate glass (Harvard Apparatus) to an open tip resistance of 4 – 5 MΩ and filled with intracellular solution containing (in mM) 130 K-Gluconate, 10 KCl, 10 HEPES, 4 Mg-ATP, 0.3 Na2-GTP, and 10 Na_2-phosphocreatine (pH 7.25, ~280 mOsm) for recordings of ChCs. Patch-clamp recordings were either performed with an Axopatch 200B (Molecular Devices) or a Dagan BVC-700A (Dagan Corporation). Signals were analogue low-pass filtered at 10 kHz (Bessel) and digitally sampled at 50 kHz using an A-D converter (ITC-18, HEKA Elektronik Dr. Schulze GmbH) and the data acquisition software Axograph X (v.1.5.4, Axograph Scientific). Bridge-balance and capacitances were fully compensated in current clamp. Series resistance was compensated to > 75% in voltage clamp. The ChCs were identified as mCyRFP-positive neurons in layer 2/3 of V1 which had a characteristic high-frequency firing pattern (Fig. 1G). Biocytin (3 mg/ml, Sigma-Aldrich) was routinely added to the intracellular solution to allow for post-hoc confirmation of cell morphology and localization (Fig. 1F).

Optogenetic stimulation

For mapping of RSC inputs to ChCs, we patched ChCs that were surrounded by a high density of eYFP+ axons. We flashed brief pulses of blue light (10% laser power, resulting in an output intensity of 5.7 mW) with the 470 nm laser line of a laser diode illuminator (LDI-7, 89 North, USA) through the imaging objective above the cell soma and apical dendrites. We recorded the postsynaptic currents in voltage-clamp mode with a –60 mV holding potential and postsynaptic potentials (PSPs) were acquired in current clamp mode at $I = 0$ holding. For confirmation of monosynaptic inputs (*38*), we first washed in TTX to the bath (5 min.) to block all action potential induced synaptic release and measured the optogenetically induced PSPs. Next, we applied for 5 minutes the specific sodium channel blocker tetrodotoxin (TTX, 500 nM, Tocris) in combination with potassium channel blocker 4-aminopyridine (4-AP, 1 mM, Tocris) to facilitate transmitter release at monosynaptic connections from RSC to ChC and recorded the PSP amplitudes (Fig. 1H). For characterization of the synaptic connection type (facilitating or depressing) we stimulated with a series of five pulses (5ms, 20Hz). We made use of an AAV9-serotyped vector, which has been shown to prevent the artificial synaptic depression during repeated optogenetic stimulation that can occur using other AAV serotypes (*93*).

Paired recordings

For paired recordings, we first established a ChC recording and then made patch-clamp recording from a nearby pyramidal cells (PyC) within <50 µm which showed also visually identified bouton cartridges. Pyramidal neurons were filled with high chloride internal solution containing (in mM) 70 K-Gluconate, 70 KCl, 0.5 EGTA, 10 HEPES, 4 MgATP, 4 K-phosphocreatine, 0.4 GTP, pH 7.3 adjusted with KOH, 285 mOsmol. Next, we evoked single APs in one

cell type with brief current injections (3 ms) and recorded PSPs in the other at their resting membrane potential (I = 0). Afterwards the stimulation of APs was switched to the other neuron to determine reciprocal connectivity. Only responses with 2x the SD of baseline noise (typically 50 µV) were considered being connected.

Histology and AIS plasticity quantification

For ChC bouton quantification we used 5 naive and 3 trained mice injected with AAV9-CaMKII-GCaMP6f and AAV5-hSyn1-flex-ChrimsonR-tdTomato. For AIS quantification we used an additional two trained mice injected with AAV9-CaMKII-GCaMP6f and AAV1-CAG-flex-mRuby2-GCaMP6f. Mice were perfused with 15 ml of ice-cold PBS followed by 30 ml of 4% paraformaldehyde (PFA). The brains were extracted and post-fixed for 2 hours in 4% PFA at 4°C. Brain were cut in 50 µm slices and selected for staining such that there was ~200 µm between slices. A total of 2 to 3 slices containing V1 were used for staining per mouse. We used the following antibodies: Guinea pig-anti-RFP (Synaptic Systems, #390004, 1:500), Rabbit-β-IV-Spectrin (Biotrend, provided by Maren Engelhardt, 1:500), Goat-anti-guinea pig Alexa Fluor 594 (Thermofisher, #A11076, 1:1000), Goat-anti-rabbit Alexa Fluor 647 (Thermofisher, #A32733, 1:1000). For the staining, slices were blocked for 90 min in 10% normal goat serum (NGS) and 0.5% Triton in PBS followed by incubation in primary antibodies overnight (5% NGS and 0.5% Triton in PBS). After three washing steps the slices were incubated with secondary antibodies for 120 min at room temperature. After three more washing steps slices were mounted on SuperFrost Plus glass slides (Fisher Scientific) using fluorescence-preserving mounting medium (Vectashield). Imaging was performed with a Leica SP8 confocal microscope using a 63x N.A. 1.40 oil-immersion objective at a frame size of 1024 x 1024 pixels. We collected z-stack images at 0.5 µm steps. Z-stacked images were processed in Neurolucida (MBF Bioscience) and AISs and ChC boutons were manually traced. We only included AISs that had a clear beginning and end.

Retrograde tracing

Adult Vipr2-Cre mice were unilaterally injected with 90 nl of AAV5-hDlx-DIO-eYFP-t2A-TVA and AAV9-hDlx-DIO-oG(*34*) in V1 (2.8 mm lateral and 0.5 mm anterior from lambda at a depth of 300 µm) followed by RabV-envA-mCherry 26 days later. After 7 days, mice were perfused as described above and their brains post-fixed overnight in 4% PFA at 4°C. After cryoprotection (48 h in 30% sucrose at 4°C) and snap freezing in liquid nitrogen slices were stored at -80°C before sectioning. We made 75 µm thick coronal slices using a cryostat (CM3050 S, Leica) and mounted sections on superFrost Plus glass slides (Fisher Scientific) using Vectashield mounting medium. Imaging for quantification was performed with an Axioscan.Z1 slide scanner (ZEISS, Germany) at 20x and a Leica SP8 confocal microscope using a 40x (NA 1.4) and 63x (NA 1.40) oil-immersion objective at a resolution of 1024x1024.

To quantify the mCherry+ input cells, we followed the QUINT workflow(*94*). First, we manually inspected and organized individual images using QuPath and converted them from .czi to .png and .tif in MATLAB. Next, we trained a pixel/object classifier in Ilastik (*95*) on a representative subset of images from each mouse and used it to subsequently segment all images for all mice. The output from Ilastik was then recolored using ImageJ. Finally, we

registered the slice images to the Allen Brain Reference Atlas using quickNII(*96*) and quantified them using Nutil and MATLAB.

Statistical analysis

All statistical details for each experiment are shown in figures and figure legends and in **Table S1**. Statistics on slice physiology experiments were performed using Prism9 (GraphPad Software). All other statistical analyses were performed using Linear Mixed Effects Models (LMEM, 'fitlme' function in MATLAB) or permutation tests. For LMEM, we considered the response parameter (e.g., visual response magnitude) as a fixed effect and session/mouse as random effect. LMEM takes into account that samples (e.g. neurons) might not be fully independent (e.g. they were obtained from the same session/mouse). We performed a one-way ANOVA on the LMEM followed by a post-hoc coefTest using Tukey's HSD to correct for multiple comparisons. Box plots represent the median, the 0.25 and 0.75 quantiles, and the 95% confidence interval (CI) of the distributions.

Resource table

Reagent or resource	**Source**	**Identifier**
Virus		
AAV9-CaMKIIa-GCaMP6f	Addgene	100834-AAV9
AAV1-CAG-flex-mRuby2-GCaMP6f	Addgene	6719-AAV1
AAV1-hSyn1-GCaMP6f	Addgene	100837-AAV1
AAV9-CaMKIIa-jGCaMP8m	VVF Zurich	v630-9
AAV-PHP.eB-shortCAG-dlox-GCaMP6f(rev)-dlox	VVF Zurich	v657-PHP.eB
AAV5-hDlx-DIO-eYFP-t2A-TVA	Dr. Seungho Lee	
AAV9-hDlx-DIO-oG	Dr. Seungho Lee	
Rbv-ΔG-mCherry	Charite Berlin	BRABV-001
AAV1-hDlx-dlox-hKORD-mCyRFP1(rev)-dlox	VVF Zurich	v326-1
AAV1-hDlx-dlox-mCyRFP1(rev)-dlox	VVF Zurich	v313-1
AAV9-CaMKIIa-ChR2-eYFP	Addgene	26969-AAV9
AAV1-hDlx-dlox-ChrimsonR-tdTomato(rev)-dlox	VVF Zurich	v674-1
Mouse strains		
Vipr2-Cre	Jackson Laboratories	031332
Pvalb-T2A-FLpO-D	Jackson Laboratories	022730
AI65(RCFL-tdT)-D	Jackson Laboratories	021875
Rbp4-Cre	GENSAT project	KL100

References

1. M. M. Karnani, J. Jackson, I. Ayzenshtat, A. Hamzehei Sichani, K. Manoocheri, S. Kim, R. Yuste, Opening Holes in the Blanket of Inhibition: Localized Lateral Disinhibition by VIP Interneurons. *J. Neurosci.* **36**, 3471–3480 (2016).

2. L. Kirchberger, S. Mukherjee, M. W. Self, P. R. Roelfsema, Contextual drive of neuronal responses in mouse V1 in the absence of feedforward input. *Sci. Adv.* **9**, eadd2498 (2023).

3. L. Kirchberger, S. Mukherjee, U. H. Schnabel, E. H. van Beest, A. Barsegyan, C. N. Levelt, J. A. Heimel, J. A. M. Lorteije, C. van der Togt, M. W. Self, P. R. Roelfsema, The essential role of recurrent processing for figure-ground perception in mice. *Sci. Adv.* **7**, eabe1833 (2021).

4. C. K. Pfeffer, M. Xue, M. He, Z. J. Huang, M. Scanziani, Inhibition of inhibition in visual cortex: the logic of connections between molecularly distinct interneurons. *Nat Neurosci*. **16**, 1068–1076 (2013).

5. D. van Versendaal, C. N. Levelt, Inhibitory interneurons in visual cortical plasticity. *Cell. Mol. Life Sci.* **73**, 3677–3691 (2016).

6. S. Zhang, M. Xu, T. Kamigaki, J. P. Hoang Do, W.-C. Chang, S. Jenvay, K. Miyamichi, L. Luo, Y. Dan, Long-range and local circuits for top-down modulation of visual cortex processing. *Science*. **345**, 660–665 (2014).

7. A. Attinger, B. Wang, G. B. Keller, Visuomotor Coupling Shapes the Functional Development of Mouse Visual Cortex. *Cell*. **169**, 1291-1302.e14 (2017).

8. H. Adesnik, W. Bruns, H. Taniguchi, Z. J. Huang, M. Scanziani, A neural circuit for spatial summation in visual cortex. *Nature*. **490**, 226–231 (2012).

9. A. J. Keller, M. Dipoppa, M. M. Roth, M. S. Caudill, A. Ingrosso, K. D. Miller, M. Scanziani, A Disinhibitory Circuit for Contextual Modulation in Primary Visual Cortex. *Neuron*. **108**, 1181-1193.e8 (2020).

10. Y. Fu, J. M. Tucciarone, J. S. Espinosa, N. Sheng, D. P. Darcy, R. A. Nicoll, Z. J. Huang, M. P. Stryker, A Cortical Circuit for Gain Control by Behavioral State. *Cell*. **156**, 1139–1152 (2014).

11. A. Peters, C. C. Proskauer, C. E. Ribak, Chandelier cells in rat visual cortex. *J. Comp. Neurol.* **206**, 397–416 (1982).

12. E. G. Jones, Varieties and distribution of non-pyramidal cells in the somatic sensory cortex of the squirrel monkey. *J. Comp. Neurol.* **160**, 205–267 (1975).

13. C. M. Schneider-Mizell, A. L. Bodor, F. Collman, D. Brittain, A. Bleckert, S. Dorkenwald, N. L. Turner, T. Macrina, K. Lee, R. Lu, J. Wu, J. Zhuang, A. Nandi, B. Hu, J. Buchanan, M. M. Takeno, R. Torres, G. Mahalingam, D. J. Bumbarger, Y. Li, T. Chartrand, N. Kemnitz, W. M. Silversmith, D. Ih, J. Zung, A. Zlateski, I. Tartavull, S. Popovych, W. Wong, M. Castro, C. S. Jordan, E. Froudarakis, L. Becker, S. Suckow, J. Reimer, A. S. Tolias, C. A. Anastassiou, H. S. Seung, R. C. Reid, N. M. da Costa, Structure and function of axo-axonic inhibition. *eLife*. **10**, e73783 (2021).

14. B. Tasic, Z. Yao, L. T. Graybuck, K. A. Smith, T. N. Nguyen, D. Bertagnolli, J. Goldy, E. Garren, M. N. Economo, S. Viswanathan, O. Penn, T. Bakken, V. Menon, J. Miller, O. Fong, K. E. Hirokawa, K. Lathia, C. Rimorin, M. Tieu, R. Larsen, T. Casper, E. Barkan, M. Kroll, S. Parry, N. V. Shapovalova, D. Hirschstein, J. Pendergraft, H. A. Sullivan, T. K. Kim, A. Szafer, N. Dee, P. Groblewski, I. Wickersham, A. Cetin, J. A. Harris, B. P. Levi, S. M. Sunkin, L. Madisen, T. L. Daigle, L. Looger, A. Bernard, J. Phillips, E. Lein, M. Hawrylycz, K. Svoboda, A. R. Jones, C. Koch, H. Zeng, Shared and distinct transcriptomic cell types across neocortical areas. *Nature*. **563**, 72–78 (2018).

15. P. Somogyi, A specific 'axo-axonal' interneuron in the visual cortex of the rat. *Brain Research*. **136**, 345–350 (1977).

16. M. H. P. Kole, G. J. Stuart, Signal Processing in the Axon Initial Segment. *Neuron*. **73**, 235–247 (2012).

17. J. M. Veres, G. A. Nagy, V. K. Vereczki, T. Andrási, N. Hájos, Strategically Positioned Inhibitory Synapses of Axo-axonic Cells Potently Control Principal Neuron Spiking in the Basolateral Amygdala. *J. Neurosci.* **34**, 16194–16206 (2014).

18. A. Pan-Vazquez, W. Wefelmeyer, V. Gonzalez Sabater, G. Neves, J. Burrone, Activity-Dependent Plasticity of Axo-axonic Synapses at the Axon Initial Segment. *Neuron*. **106**, 265-276.e6 (2020).

19. J. Szabadics, C. Varga, G. Molnár, S. Oláh, P. Barzó, G. Tamás, Excitatory Effect of GABAergic Axo-Axonic Cells in Cortical Microcircuits. *Science*. **311**, 233–235 (2006).

20. A. Woodruff, Depolarizing effect of neocortical chandelier neurons. *Front. Neural Circuits*. **3** (2009), doi:10.3389/neuro.04.015.2009.

21. A. R. Woodruff, L. M. McGarry, T. P. Vogels, M. Inan, S. A. Anderson, R. Yuste, State-Dependent Function of Neocortical Chandelier Cells. *Journal of Neuroscience*. **31**, 17872–17886 (2011).

22. A. R. Woodruff, S. A. Anderson, R. Yuste, The Enigmatic Function of Chandelier Cells. *Front. Neurosci.* **4** (2010), doi:10.3389/fnins.2010.00201.

23. L. L. Glickfeld, J. D. Roberts, P. Somogyi, M. Scanziani, Interneurons hyperpolarize pyramidal cells along their entire somatodendritic axis. *Nat Neurosci*. **12**, 21–23 (2009).

24. G. Molnár, S. Oláh, G. Komlósi, M. Füle, J. Szabadics, C. Varga, P. Barzó, G. Tamás, Complex Events Initiated by Individual Spikes in the Human Cerebral Cortex. *PLoS Biol*. **6**, e222 (2008).

25. Y. Murata, M. T. Colonnese, GABAergic interneurons excite neonatal hippocampus in vivo. *Sci. Adv.* **6**, eaba1430 (2020).

26. J. Lu, J. Tucciarone, N. Padilla-Coreano, M. He, J. A. Gordon, Z. J. Huang, Selective inhibitory control of pyramidal neuron ensembles and cortical subnetworks by chandelier cells. *Nat Neurosci*. **20**, 1377–1383 (2017).

27. B. Dudok, M. Szoboszlay, A. Paul, P. M. Klein, Z. Liao, E. Hwaun, G. G. Szabo, T. Geiller, B. Vancura, B.-S. Wang, S. McKenzie, J. Homidan, L. M. F. Klaver, D. F. English, Z. J. Huang, G. Buzsáki, A. Losonczy, I. Soltesz, Recruitment and inhibitory action of hippocampal axo-axonic cells during behavior. *Neuron*. **109**, 3838-3850.e8 (2021).

28. K. Jung, Y. Choi, H.-B. Kwon, Cortical control of chandelier cells in neural codes. *Front. Cell. Neurosci.* **16**, 992409 (2022).

29. S. Bugeon, J. Duffield, M. Dipoppa, A. Ritoux, I. Prankerd, D. Nicoloutsopoulos, D. Orme, M. Shinn, H. Peng, H. Forrest, A. Viduolyte, C. B. Reddy, Y. Isogai, M. Carandini, K. D. Harris, A transcriptomic axis predicts state modulation of cortical interneurons. *Nature*. **607**, 330–338 (2022).

30. T. C. M. Bienvenu, D. Busti, P. J. Magill, F. Ferraguti, M. Capogna, Cell-Type-Specific Recruitment of Amygdala Interneurons to Hippocampal Theta Rhythm and Noxious Stimuli In Vivo. *Neuron*. **74**, 1059–1074 (2012).

31. L. Massi, M. Lagler, K. Hartwich, Z. Borhegyi, P. Somogyi, T. Klausberger, Temporal Dynamics of Parvalbumin-Expressing Axo-axonic and Basket Cells in the Rat Medial Prefrontal Cortex In Vivo. *Journal of Neuroscience*. **32**, 16496–16502 (2012).

32. B.-S. Wang, M. S. Bernardez Sarria, X. An, M. He, N. M. Alam, G. T. Prusky, M. C. Crair, Z. J. Huang, Retinal and Callosal Activity-Dependent Chandelier Cell Elimination Shapes Binocularity in Primary Visual Cortex. *Neuron*. **109**, 502-515.e7 (2021).

33. T. L. Daigle, L. Madisen, T. A. Hage, M. T. Valley, U. Knoblich, R. S. Larsen, M. M. Takeno, L. Huang, H. Gu, R. Larsen, M. Mills, A. Bosma-Moody, L. A. Siverts, M. Walker, L. T. Graybuck, Z. Yao, O. Fong, T. N. Nguyen, E. Garren, G. H. Lenz, M. Chavarha, J. Pendergraft, J. Harrington, K. E. Hirokawa, J. A. Harris, P. R. Nicovich, M. J. McGraw, D. R. Ollerenshaw, K. A. Smith, C. A. Baker, J. T. Ting, S. M. Sunkin, J. Lecoq, M. Z. Lin, E. S. Boyden, G. J. Murphy, N. M. da Costa, J. Waters, L. Li, B. Tasic, H. Zeng, A Suite of Transgenic Driver and Reporter Mouse Lines with Enhanced Brain-Cell-Type Targeting and Functionality. *Cell*. **174**, 465-480.e22 (2018).

34. S. Lee, J.-H. Kim, Basal Forebrain Cholinergic-induced Activation of Cholecystokinin Inhibitory Neurons in the Basolateral Amygdala. *Exp Neurobiol*. **28**, 320–328 (2019).

35. H. Taniguchi, M. He, P. Wu, S. Kim, R. Paik, K. Sugino, D. Kvitsani, Y. Fu, J. Lu, Y. Lin, G. Miyoshi, Y. Shima, G. Fishell, S. B. Nelson, Z. J. Huang, A Resource of Cre Driver Lines for Genetic Targeting of GABAergic Neurons in Cerebral Cortex. *Neuron*. **71**, 995–1013 (2011).

36. G. Ma, Y. Liu, L. Wang, Z. Xiao, K. Song, Y. Wang, W. Peng, X. Liu, Z. Wang, S. Jin, Z. Tao, C. T. Li, T. Xu, F. Xu, M. Xu, S. Zhang, Hierarchy in sensory processing reflected by innervation balance on cortical interneurons. *Sci. Adv.* **7**, eabf5676 (2021).

37. X. Xu, E. M. Callaway, Laminar Specificity of Functional Input to Distinct Types of Inhibitory Cortical Neurons. *Journal of Neuroscience*. **29**, 70–85 (2009).

38. S. J. Cruikshank, H. Urabe, A. V. Nurmikko, B. W. Connors, Pathway-Specific Feedforward Circuits between Thalamus and Neocortex Revealed by Selective Optical Stimulation of Axons. *Neuron*. **65**, 230–245 (2010).

39. R. S. Zucker, W. G. Regehr, Short-Term Synaptic Plasticity. *Annu. Rev. Physiol.* **64**, 355–405 (2002).

40. X. Jiang, S. Shen, C. R. Cadwell, P. Berens, F. Sinz, A. S. Ecker, S. Patel, A. S. Tolias, Principles of connectivity among morphologically defined cell types in adult neocortex. *Science*. **350**, aac9462 (2015).

41. G. Felsen, Y. Dan, A natural approach to studying vision. *Nat Neurosci*. **8**, 1643–1646 (2005).

42. S. A. Cadena, G. H. Denfield, E. Y. Walker, L. A. Gatys, A. S. Tolias, M. Bethge, A. S. Ecker, Deep convolutional models improve predictions of macaque V1 responses to natural images. *PLoS Comput Biol*. **15**, e1006897 (2019).

43. E. Y. Walker, F. H. Sinz, E. Cobos, T. Muhammad, E. Froudarakis, P. G. Fahey, A. S. Ecker, J. Reimer, X. Pitkow, A. S. Tolias, Inception loops discover what excites neurons most using deep predictive models. *Nat Neurosci*. **22**, 2060–2065 (2019).

44. P. Bashivan, K. Kar, J. J. DiCarlo, Neural population control via deep image synthesis. *Science*. **364**, eaav9436 (2019).

45. P. Papale, W. Zuiderbaan, R. R. M. Teeuwen, A. Gilhuis, M. W. Self, P. R. Roelfsema, S. O. Dumoulin, “The influence of objecthood on the representation of natural images in the visual cortex” (preprint, Neuroscience, 2021), , doi:10.1101/2021.09.21.461209.

46. Y. Zhang, M. Rózsa, Y. Liang, D. Bushey, Z. Wei, J. Zheng, D. Reep, G. J. Broussard, A. Tsang, G. Tsegaye, S. Narayan, C. J. Obara, J.-X. Lim, R. Patel, R. Zhang, M. B. Ahrens, G. C. Turner, S. S.-H. Wang, W. L. Korff, E. R. Schreiter, K. Svoboda, J. P. Hasseman, I. Kolb, L. L. Looger, Fast and sensitive GCaMP calcium indicators for imaging neural populations. *Nature*. **615**, 884–891 (2023).

47. B. E. Deverman, P. L. Pravdo, B. P. Simpson, S. R. Kumar, K. Y. Chan, A. Banerjee, W.-L. Wu, B. Yang, N. Huber, S. P. Pasca, V. Gradinaru, Cre-dependent selection yields AAV variants for widespread gene transfer to the adult brain. *Nat Biotechnol*. **34**, 204–209 (2016).

48. C. R. Gerfen, R. Paletzki, N. Heintz, GENSAT BAC Cre-Recombinase Driver Lines to Study the Functional Organization of Cerebral Cortical and Basal Ganglia Circuits. *Neuron*. **80**, 1368–1383 (2013).

49. D. Zoccolan, M. Kouh, T. Poggio, J. J. DiCarlo, Trade-Off between Object Selectivity and Tolerance in Monkey Inferotemporal Cortex. *J. Neurosci.* **27**, 12292–12307 (2007).

50. J. A. Heimel, M. H. Saiepour, S. Chakravarthy, J. M. Hermans, C. N. Levelt, Contrast gain control and cortical TrkB signaling shape visual acuity. *Nat Neurosci*. **13**, 642–648 (2010).

51. G. M. Boynton, J. B. Demb, G. H. Glover, D. J. Heeger, Neuronal basis of contrast discrimination. *Vision Research*. **39**, 257–269 (1999).

52. S. M. O’Toole, H. K. Oyibo, G. B. Keller, “Prediction error neurons in mouse cortex are molecularly targetable cell types” (preprint, Neuroscience, 2022), , doi:10.1101/2022.07.20.500837.

53. R. Jordan, G. B. Keller, Opposing Influence of Top-down and Bottom-up Input on Excitatory Layer 2/3 Neurons in Mouse Primary Visual Cortex. *Neuron*. **108**, 1194-1206.e5 (2020).

54. G. B. Keller, T. Bonhoeffer, M. Hübener, Sensorimotor Mismatch Signals in Primary Visual Cortex of the Behaving Mouse. *Neuron*. **74**, 809–815 (2012).

55. P. Zmarz, G. B. Keller, Mismatch Receptive Fields in Mouse Visual Cortex. *Neuron*. **92**, 766–772 (2016).

56. R. Jordan, G. B. Keller, “The locus coeruleus broadcasts prediction errors across the cortex to promote sensorimotor plasticity” (preprint, elife, 2023), , doi:10.7554/eLife.85111.1.

57. T. Muzzu, A. B. Saleem, Feature selectivity can explain mismatch signals in mouse visual cortex. *Cell Reports*. **37**, 109772 (2021).

58. H. Taniguchi, J. Lu, Z. J. Huang, The Spatial and Temporal Origin of Chandelier Cells in Mouse Neocortex. *Science*. **339**, 70–74 (2013).

59. H. Kuba, Y. Oichi, H. Ohmori, Presynaptic activity regulates Na+ channel distribution at the axon initial segment. *Nature*. **465**, 1075–1078 (2010).

60. N. Jamann, D. Dannehl, N. Lehmann, R. Wagener, C. Thielemann, C. Schultz, J. Staiger, M. H. P. Kole, M. Engelhardt, Sensory input drives rapid homeostatic scaling of the axon initial segment in mouse barrel cortex. *Nat Commun*. **12**, 23 (2021).

61. M. S. Grubb, J. Burrone, Activity-dependent relocation of the axon initial segment fine-tunes neuronal excitability. *Nature*. **465**, 1070–1074 (2010).

62. A. Gutzmann, N. ErgÃ¼l, R. Grossmann, C. Schultz, P. Wahle, M. Engelhardt, A period of structural plasticity at the axon initial segment in developing visual cortex. *Front. Neuroanat.* **8** (2014), doi:10.3389/fnana.2014.00011.

63. W. Wefelmeyer, D. Cattaert, J. Burrone, Activity-dependent mismatch between axo-axonic synapses and the axon initial segment controls neuronal output. *Proc. Natl. Acad. Sci. U.S.A.* **112**, 9757–9762 (2015).

64. E. Vardy, J. E. Robinson, C. Li, R. H. J. Olsen, J. F. DiBerto, P. M. Giguere, F. M. Sassano, X.-P. Huang, H. Zhu, D. J. Urban, K. L. White, J. E. Rittiner, N. A. Crowley, K. E. Pleil, C. M. Mazzone, P. D. Mosier, J. Song, T. L. Kash, C. J. Malanga, M. J. Krashes, B. L. Roth, A New DREADD Facilitates the Multiplexed Chemogenetic Interrogation of Behavior. *Neuron*. **86**, 936–946 (2015).

65. M. Heindorf, G. B. Keller, "Reduction of layer 5 mediated long-range cortical communication by antipsychotic drugs" (preprint, Neuroscience, 2022), , doi:10.1101/2022.01.31.478462.

66. A. Steinecke, M. M. Bolton, H. Taniguchi, Neuromodulatory control of inhibitory network arborization in the developing postnatal neocortex. *Sci. Adv.* **8**, eabe7192 (2022).

67. Y. Kawaguchi, T. Shindou, Noradrenergic Excitation and Inhibition of GABAergic Cell Types in Rat Frontal Cortex. *J. Neurosci.* **18**, 6963–6976 (1998).

68. K. Friston, Prediction, perception and agency. *International Journal of Psychophysiology*. **83**, 248–252 (2012).

69. R. P. N. Rao, D. H. Ballard, Predictive coding in the visual cortex: a functional interpretation of some extra-classical receptive-field effects. *Nat Neurosci*. **2**, 79–87 (1999).

70. S. Shipp, Neural Elements for Predictive Coding. *Front. Psychol.* **7** (2016), doi:10.3389/fpsyg.2016.01792.

71. C. Summerfield, V. Wyart, V. M. Johnen, V. de Gardelle, Human Scalp Electroencephalography Reveals that Repetition Suppression Varies with Expectation. *Front. Hum. Neurosci.* **5** (2011), doi:10.3389/fnhum.2011.00067.

72. H. E. M. den Ouden, P. Kok, F. P. de Lange, How Prediction Errors Shape Perception, Attention, and Motivation. *Front. Psychology*. **3** (2012), doi:10.3389/fpsyg.2012.00548.

73. T. S. Lee, D. Mumford, Hierarchical Bayesian inference in the visual cortex. *J. Opt. Soc. Am. A*. **20**, 1434 (2003).

74. G. B. Keller, T. D. Mrsic-Flogel, Predictive Processing: A Canonical Cortical Computation. *Neuron*. **100**, 424–435 (2018).

75. Egner, T., & Summerfield, C., Grounding predictive coding models in empirical neuroscience research. *Behavioral and Brain Sciences*. **36**, 210–211 (2013).

76. A. M. Bastos, W. M. Usrey, R. A. Adams, G. R. Mangun, P. Fries, K. J. Friston, Canonical Microcircuits for Predictive Coding. *Neuron*. **76**, 695–711 (2012).

77. N. B. Gallo, A. Paul, L. Van Aelst, Shedding Light on Chandelier Cell Development, Connectivity, and Contribution to Neural Disorders. *Trends in Neurosciences*. **43**, 565–580 (2020).

78. R. J. Douglas, K. A. C. Martin, Control of Neuronal Output by Inhibition at the Axon Initial Segment. *Neural Computation*. **2**, 283–292 (1990).

79. Z. Shang, J. Huang, N. Liu, X. Zhang, Bi-directional Control of Synaptic Input Summation and Spike Generation by GABAergic Inputs at the Axon Initial Segment. *Neurosci. Bull.* **39**, 1–13 (2023).

80. I. Benedeczky, E. Molnár, P. Somogyi, The cisternal organelle as a Ca2+-storing compartment associated with GABAergic synapses in the axon initial segment of hippocampal pyramidal neurones. *Exp Brain Res*. **101**, 216–230 (1994).

81. A. Schlüter, D. Del Turco, T. Deller, A. Gutzmann, C. Schultz, M. Engelhardt, Structural Plasticity of Synaptopodin in the Axon Initial Segment during Visual Cortex Development. *Cerebral Cortex*. **27**, 4662–4675 (2017).

82. C. Thome, J. M. Janssen, S. Karabulut, C. Acuna, E. D'Este, S. J. Soyka, K. Baum, M. Bock, N. Lehmann, M. Hasegawa, D. A. Ganea, C. M. Benoit, J. Gründemann, C. Schultz, V. Bennett, P. M. Jenkins, M. Engelhardt, "Live imaging of excitable axonal microdomains in ankyrin-G-GFP mice" (preprint, Neuroscience, 2023), , doi:10.1101/2023.02.01.525891.

83. M. N. Hebart, A. H. Dickter, A. Kidder, W. Y. Kwok, A. Corriveau, C. Van Wicklin, C. I. Baker, THINGS: A database of 1,854 object concepts and more than 26,000 naturalistic object images. *PLoS ONE*. **14**, e0223792 (2019).

84. L. de Kraker, K. Seignette, P. Thamizharasu, B. J. G. van den Boom, I. Ferreira Pica, I. Willuhn, C. N. Levelt, C. van der Togt, SpecSeg is a versatile toolbox that segments neurons and neurites in chronic calcium imaging datasets based on low-frequency cross-spectral power. *Cell Reports Methods*. **2**, 100299 (2022).

85. E. A. Pnevmatikakis, A. Giovannucci, NoRMCorre: An online algorithm for piecewise rigid motion correction of calcium imaging data. *Journal of Neuroscience Methods*. **291**, 83–94 (2017).

86. P. Rupprecht, S. Carta, A. Hoffmann, M. Echizen, A. Blot, A. C. Kwan, Y. Dan, S. B. Hofer, K. Kitamura, F. Helmchen, R. W. Friedrich, A database and deep learning toolbox for noise-optimized, generalized spike inference from calcium imaging. *Nat Neurosci*. **24**, 1324–1337 (2021).

87. C. Szegedy, W. Liu, Y. Jia, P. Sermanet, S. Reed, D. Anguelov, D. Erhan, V. Vanhoucke, A. Rabinovich, Going Deeper with Convolutions (2014), (available at http://arxiv.org/abs/1409.4842).

88. A. Paszke, S. Gross, S. Chintala, G. Chanan, E. Yang, Z. DeVito, Z. Lin, A. Desmaison, L. Antiga, A. Lerer, Automatic differentiation in PyTorch.

89. D. P. Kingma, J. Ba, Adam: A Method for Stochastic Optimization (2017), (available at http://arxiv.org/abs/1412.6980).

90. Olah, et al., "Feature Visualization", Distill, 2017.

91. A. B. Saleem, E. M. Diamanti, J. Fournier, K. D. Harris, M. Carandini, Coherent encoding of subjective spatial position in visual cortex and hippocampus. *Nature*. **562**, 124–127 (2018).

92. A. Fiser, D. Mahringer, H. K. Oyibo, A. V. Petersen, M. Leinweber, G. B. Keller, Experience-dependent spatial expectations in mouse visual cortex. *Nat Neurosci*. **19**, 1658–1664 (2016).

93. S. L. Jackman, B. M. Beneduce, I. R. Drew, W. G. Regehr, Achieving High-Frequency Optical Control of Synaptic Transmission. *J. Neurosci.* **34**, 7704–7714 (2014).

94. S. C. Yates, N. E. Groeneboom, C. Coello, S. F. Lichtenthaler, P.-H. Kuhn, H.-U. Demuth, M. Hartlage-Rübsamen, S. Roßner, T. Leergaard, A. Kreshuk, M. A. Puchades, J. G. Bjaalie, QUINT: Workflow for Quantification and Spatial Analysis of Features in Histological Images From Rodent Brain. *Front. Neuroinform.* **13**, 75 (2019).

95. S. Berg, D. Kutra, T. Kroeger, C. N. Straehle, B. X. Kausler, C. Haubold, M. Schiegg, J. Ales, T. Beier, M. Rudy, K. Eren, J. I. Cervantes, B. Xu, F. Beuttenmueller, A. Wolny, C. Zhang, U. Koethe, F. A. Hamprecht, A. Kreshuk, ilastik: interactive machine learning for (bio)image analysis. *Nat Methods*. **16**, 1226–1232 (2019).

96. M. A. Puchades, G. Csucs, D. Ledergerber, T. B. Leergaard, J. G. Bjaalie, Spatial registration of serial microscopic brain images to three-dimensional reference atlases with the QuickNII tool. *PLoS ONE*. **14**, e0216796 (2019).

Acknowledgments

We thank all members of the Levelt lab for discussion and support. We thank staff of the animal facility and mechatronics department at the Netherlands Institute for Neuroscience for technical support. We thank Dr. Seungho Lee from Pohang University of Science and Technology for kindly providing viral vectors for rabies tracing experiments and Dr. Hongkui Zeng and the Allen Institute for Brain Science for providing the Vipr2-Cre mice. We thank Dr. Maren Engelhardt for providing the Rabbit-β-IV-Spectrin antibody, Barbara Hobo for help with tail vein injections, Ulrike Schlegel for help with QUINT software and David van Oorschot and Dilara Ilhan for help with experiments. We are grateful to Dr. Jean-Charles Paterna and Dr. Melanie Rauch from the Viral Vector Facility VVF at the ETH Zurich and University of Zurich for their expert advice, support and services regarding viral vector production. This project received funding from the European Union's Horizon 2020 Research and Innovation Program under grant agreement nos. 785907 (HBP SGA2, CL & PR) and 945539 (HBP SGA3, CL & PR), from the Dutch Research Council (NWO-OCENW.KLEIN.178, CL & PR and FlagEra SoundSight, 680-91-320, CL). The authors declare that they have no competing interests. All data needed to evaluate the conclusions in the paper are present in the paper and/or the Supplementary Materials.

Author contributions

	KS	NJ	PP	HT	RPOP	LK	CT	MA	MWS	JSM	ER	PN	PRR	MHPK	CNL
Experimental design	X	X	X											X	X
Data collection	X	X		X	X			X							
Data analysis	X	X	X	X	X	X	X		X	X					
Data curation							X								
Technical assistance											X	X			
Interpretation	X	X	X											X	X
Writing	X	X	X												X
Review/editing	X	X	X	X	X	X	X	X	X	X			X	X	X
Conceptualization	X														X
Funding acquisition															X

Supplementary Materials

Table S1. Statistics

Figure		Comparison	Parameter	Test	# mice	# sessions	N represents	Nr of neurons	p-val	Sign
1	**C**	NA	Nr of starter cells (mean+-sem)	NA	4	NA	Starters	7.5 +- 3.8	NA	NA
	H	Ctrl/TTX/TTX+4-AP	Amplitude	RM Anova (Holm-Sidak's)			Neurons	11	0.0035	**
		Ctrl vs TTX	Amplitude	RM Anova (Holm-Sidak's)			Neurons	11	0.012	*
		TTX vs TTX+4-AP	Amplitude	RM Anova (Holm-Sidak's)			Neurons	11	0.008	**
2	**C**	PyCs vs ChCs	Running speed correlation	LMEM-Anova	8	15	Neurons	1883 vs 95	<0.001	***
		PyCs vs ChCs	Pupil area correlation	LMEM-Anova	8	15	Neurons	1883 vs 95	<0.001	***
		PyCs vs ChCs	Within group correlation	LMEM-Anova	8	15	Neurons	1883 vs 95	<0.001	***
	E	PyC vs ChC	Response strength	LMEM-Anova	8	15	Neurons	1883 vs 95	0.2946	ns
	G	PyC vs ChC	OSI	LMEM-Anova	8	15	Neurons	1883 vs 95	<0.001	***
		PyC vs ChC	DSI	LMEM-Anova	8	15	Neurons	1883 vs 95	0.9629	ns
3	**B**	Overall cell type	Response strength	LMEM-Anova	10	11	Neurons	2650	0.1461	ns
		L23 PyCs vs L5 PyCs	Response strength	LMEM-Tukey	4 vs 6	5 vs 6	Neurons	1015 vs 34	0.5922	ns
		L23 PyCs vs ChCs	Response strength	LMEM-Tukey	4 vs 4	5 vs 5	Neurons	1015 vs 1601	0.1847	ns
		L5 PyCs vs ChCs	Response strength	LMEM-Tukey	6 vs 4	6 vs 5	Neurons	34 vs 1601	0.9999	ns
	C	Overall cell type	Sparsity	LMEM-Anova	9	10	Neurons	2493	<0.001	***
		L23 PyCs vs L5 PyCs	Sparsity	LMEM-Tukey	4 vs 5	5 vs 5	Neurons	1015 vs 1444	0.3303	ns
		L23 PyCs vs ChCs	Sparsity	LMEM-Tukey	4 vs 4	5 vs 5	Neurons	1015 vs 34	<0.001	***
		L5 PyCs vs ChCs	Sparsity	LMEM-Tukey	5 vs 4	5 vs 5	Neurons	34 vs 1601	<0.001	***
	D	Overall cell type	Correlation between cells	LMEM-Anova	10	11	Neurons	2650,00	<0.001	***
		L23 PyCs vs L5 PyCs	Correlation between cells	LMEM-Tukey	4 vs 6	5 vs 6	Neurons	1015 vs 1601	<0.001	***
		L23 PyCs vs ChCs	Correlation between cells	LMEM-Tukey	4 vs 4	5 vs 5	Neurons	1015 vs 34	<0.001	***
		L5 PyCs vs ChCs	Correlation between cells	LMEM-Tukey	6 vs 4	6 vs 5	Neurons	34 vs 1601	<0.001	***
	E	L23 PyCs vs ChCs	Decoding accuracy	Permutation test	4	5	Neurons	34 vs 34	<0.001	***
	G	Overall cell type	OSI	LMEM-Anova	9	10	Neurons	2111	0.0025	**
		L23 PyCs vs L5 PyCs	OSI	LMEM-Tukey	4 vs 5	5 vs 5	Neurons	922 vs 1163	0.9999	ns
		L23 PyCs vs ChCs	OSI	LMEM-Tukey	4 vs 4	5 vs 5	Neurons	922 vs 26	0.0011	**
		L5 PyCs vs ChCs	OSI	LMEM-Tukey	5 vs 4	5 vs 5	Neurons	26 vs 1163	0.0034	**
	H	Overall cell type	Contrast sensitivity	LMEM-Anova	9	10	Neurons	2111	<0.001	***
		L23 PyCs vs L5 PyCs	Contrast sensitivity	LMEM-Tukey	4 vs 5	5 vs 5	Neurons	922 vs 1163	0.0037	**
		L23 PyCs vs ChCs	Contrast sensitivity	LMEM-Tukey	4 vs 4	5 vs 5	Neurons	922 vs 26	<0.001	***
		L5 PyCs vs ChCs	Contrast sensitivity	LMEM-Tukey	5 vs 4	5 vs 5	Neurons	26 vs 1163	<0.001	***
	I	Overall cell type	SF	LMEM-Anova	9	10	Neurons	2111	<0.001	***
		L23 PyCs vs L5 PyCs	SF	LMEM-Tukey	4 vs 5	5 vs 5	Neurons	922 vs 1163	<0.001	***
		L23 PyCs vs ChCs	SF	LMEM-Tukey	4 vs 4	5 vs 5	Neurons	922 vs 26	0.2679	ns
		L5 PyCs vs ChCs	SF	LMEM-Tukey	5 vs 4	5 vs 5	Neurons	26 vs 1163	0.0033	**
	J	Overall cell type	RF size	LMEM-Anova	9	10	Neurons	2081	0.0182	*
		L23 PyCs vs L5 PyCs	RF size	LMEM-Tukey	4 vs 5	5 vs 5	Neurons	908 vs 1147	0.2527	ns
		L23 PyCs vs ChCs	RF size	LMEM-Tukey	4 vs 4	5 vs 5	Neurons	908 vs 26	0.0304	*
		L5 PyCs vs ChCs	RF size	LMEM-Tukey	5 vs 4	5 vs 5	Neurons	26 vs 1147	0.7453	ns
S2	**B**	Overall cell type	Oracle correlation	LMEM-Anova	10	11	Neurons	2650	<0.001	***
		L23 PyCs vs L5 PyCs	Oracle correlation	LMEM-Tukey	4 vs 6	5 vs 6	Neurons	1015 vs 34	<0.001	***
		L23 PyCs vs ChCs	Oracle correlation	LMEM-Tukey	4 vs 4	5 vs 5	Neurons	1015 vs 1601	<0.001	***
		L5 PyCs vs ChCs	Oracle correlation	LMEM-Tukey	6 vs 4	6 vs 5	Neurons	34 vs 1601	0.0177	*
	C	Overall cell type	Cross validation correlation	LMEM-Anova	10	11	Neurons	2650	<0.001	***
		L23 PyCs vs L5 PyCs	Cross validation correlation	LMEM-Tukey	4 vs 6	5 vs 6	Neurons	1015 vs 34	0.0062	**
		L23 PyCs vs ChCs	Cross validation correlation	LMEM-Tukey	4 vs 4	5 vs 5	Neurons	1015 vs 1601	<0.001	***
		L5 PyCs vs ChCs	Cross validation correlation	LMEM-Tukey	6 vs 4	6 vs 5	Neurons	34 vs 1601	0.0598	ns

4	**G**	Overall cell type	Visual	LMEM-Anova	6	12	Neurons	1290	<0.001	***
		V vs NV	Visual	LMEM-Tukey	6	12	Neurons	546 vs 710	<0.001	***
		V vs ChC	Visual	LMEM-Tukey	6	12	Neurons	546 vs 34	<0.001	***
		NV vs ChC	Visual	LMEM-Tukey	6	12	Neurons	710 vs 34	<0.001	***
	H	Overall cell type	Non-visual	LMEM-Anova	6	12	Neurons	1290	<0.001	***
		V vs NV	Non-visual	LMEM-Tukey	6	12	Neurons	546 vs 710	<0.001	***
		V vs ChC	Non-visual	LMEM-Tukey	6	12	Neurons	546 vs 34	<0.001	***
		NV vs ChC	Non-visual	LMEM-Tukey	6	12	Neurons	710 vs 34	<0.001	***
	I	Overall cell type	Mismatch	LMEM-Anova	6	12	Neurons	1290	<0.001	***
		V vs NV	Mismatch	LMEM-Tukey	6	12	Neurons	546 vs 710	<0.001	***
		V vs ChC	Mismatch	LMEM-Tukey	6	12	Neurons	546 vs 34	<0.001	***
		NV vs ChC	Mismatch	LMEM-Tukey	6	12	Neurons	710 vs 34	<0.001	***
	J	Overall cell type	Locomotion onset	LMEM-Anova	6	12	Neurons	1290	<0.001	***
		V vs NV	Locomotion onset	LMEM-Tukey	6	12	Neurons	546 vs 710	<0.001	***
		V vs ChC	Locomotion onset	LMEM-Tukey	6	12	Neurons	546 vs 34	<0.001	***
		NV vs ChC	Locomotion onset	LMEM-Tukey	6	12	Neurons	710 vs 34	<0.001	***
	K	V vs NV	Correlation with ChCs	LMEM-Anova	6	12	Neurons	546 vs 710	<0.001	***
S3	**B**	Overall cell type	Visual flow onset	LMEM-Anova	6	12	Neurons	1290	<0.001	***
		V vs NV	Visual flow onset	LMEM-Tukey	6	12	Neurons	546 vs 710	<0.001	***
		V vs ChC	Visual flow onset	LMEM-Tukey	6	12	Neurons	546 vs 34	<0.001	***
		NV vs ChC	Visual flow onset	LMEM-Tukey	6	12	Neurons	710 vs 34	<0.001	***
	F	Real vs permutation	Visual response (z-score)	Permutation test	6	12	Neurons	1290	<0.001	***
	L	Overall cell type	Visual	LMEM-Anova	2	4	Neurons	256	<0.001	***
		V vs NV	Visual	LMEM-Tukey	2	4	Neurons	104 vs 126	<0.001	***
		V vs ChC	Visual	LMEM-Tukey	2	4	Neurons	104 vs 26	<0.001	***
		NV vs ChC	Visual	LMEM-Tukey	2	4	Neurons	126 vs 26	<0.001	***
	M	Overall cell type	Non-visual	LMEM-Anova	2	4	Neurons	256	<0.001	***
		V vs NV	Non-visual	LMEM-Tukey	2	4	Neurons	104 vs 126	<0.001	***
		V vs ChC	Non-visual	LMEM-Tukey	2	4	Neurons	104 vs 26	<0.001	***
		NV vs ChC	Non-visual	LMEM-Tukey	2	4	Neurons	126 vs 26	<0.001	***
	N	Overall cell type	Mismatch	LMEM-Anova	2	4	Neurons	256	<0.001	***
		V vs NV	Mismatch	LMEM-Tukey	2	4	Neurons	104 vs 126	<0.001	***
		V vs ChC	Mismatch	LMEM-Tukey	2	4	Neurons	104 vs 26	<0.001	***
		NV vs ChC	Mismatch	LMEM-Tukey	2	4	Neurons	126 vs 26	<0.001	***
	O	Overall cell type	Locomotion onset	LMEM-Anova	2	4	Neurons	256	<0.001	***
		V vs NV	Locomotion onset	LMEM-Tukey	2	4	Neurons	104 vs 126	<0.001	***
		V vs ChC	Locomotion onset	LMEM-Tukey	2	4	Neurons	104 vs 26	<0.001	***
		NV vs ChC	Locomotion onset	LMEM-Tukey	2	4	Neurons	126 vs 26	<0.001	***
	P	Overall cell type	Visual flow onset	LMEM-Anova	2	4	Neurons	256	<0.001	***
		V vs NV	Visual flow onset	LMEM-Tukey	2	4	Neurons	104 vs 126	<0.001	***
		V vs ChC	Visual flow onset	LMEM-Tukey	2	4	Neurons	104 vs 26	<0.001	***
		NV vs ChC	Visual flow onset	LMEM-Tukey	2	4	Neurons	126 vs 26	0.0064	**
5	**D**	Naive vs Trained PyC	Visual response strength	LMEM-Anova	5	8	Neurons	411	0.1764	ns
		Naive vs Trained ChC	Visual response strength	LMEM-Anova	5	8	Neurons	51	0.0145	*
	-	Naive vs Trained PyC	OSI	LMEM-Anova	5	8	Neurons	411	0.1316	ns
	-	Naive vs Trained PyC	DSI	LMEM-Anova	5	8	Neurons	411	0.9573	ns
	-	Naive vs Trained ChC	OSI	LMEM-Anova	5	8	Neurons	51	0.2199	ns
	-	Naive vs Trained ChC	DSI	LMEM-Anova	5	8	Neurons	51	0.9774	ns
	G	Naive vs Trained V-PyC	Visual response strength	LMEM-Anova	3	5	Neurons	68	0.9822	ns
		Naive vs Trained NV-PyC	Visual response strength	LMEM-Anova	3	5	Neurons	71	0.0246	*

6	**B**	Naive vs Trained	Nr of boutons on all AIS	LMEM-Anova	5 vs 3		Neurons (AIS)	1802 vs 1007	0.1740	ns
	C	Naive vs Trained	Nr of boutons on contacted AIS	LMEM-Anova	5 vs 3		Neurons (AIS)	1200 vs 738	0.6545	ns
	D	Naive vs Trained	Fraction contacted	Chi-square	5 vs 3		Neurons (AIS)	1802 vs 1007	<0.001	***
	F	Naive vs Trained	AIS length	LMEM-Anova	5 vs 5		Neurons (AIS)	1802 vs 1556	0.0299	*
	G	Naive vs Trained	Density	LMEM-Anova	5 vs 3		Neurons (AIS)	1200 vs 738	0.0159	*
	I	Naive vs Trained	Distance from AIS base	LMEM-Anova	5 vs 3		Boutons	3906 vs 2587	<0.001	***
7	**B**	ChC	dF/F	LMEM-Anova	12	12	Neurons	84	0.0023	**
		PyC	dF/F	LMEM-Anova	12	12	Neurons	1669	<0.001	***
	D	ChC	Intercept	LMEM-Anova	12	12	Neurons	84	<0.001	***
		PyC	Intercept	LMEM-Anova	12	12	Neurons	1669	<0.001	***
	E	ChC	Slope	LMEM-Anova	12	12	Neurons	84	<0.001	***
		PyC	Slope	LMEM-Anova	12	12	Neurons	1669	0.3124	ns
	F	ChC	dF/F	LMEM-Anova	7	7	Neurons	37	0.0977	ns
		PyC	dF/F	LMEM-Anova	7	7	Neurons	968	0.8794	ns
	H	ChC	Intercept	LMEM-Anova	7	7	Neurons	37	0.1232	ns
		PyC	Intercept	LMEM-Anova	7	7	Neurons	968	0.5448	ns
	I	ChC	Slope	LMEM-Anova	7	7	Neurons	37	0.5205	ns
		PyC	Slope	LMEM-Anova	7	7	Neurons	968	0.1231	ns
	-	PyC	Correlation (run mod vs Δsig)	Corrcoef	12	12	Neurons	1669	0.7827	ns

Supplementary Movies (1-2) and Figures (1-3)

Movie S1. Example two-photon calcium imaging recording during spontaneous behavior

Example recording showing a field of view with four ChCs (red and encircled) and PyCs during spontaneous behavior. The activity of the four ChCs is shown on the right as red traces. Movie frames correspond to the ΔF/F values at the dotted line. The black trace (bottom right) indicates the running speed of the mouse. Playback speed is 2x real time. Note the correlation between ChCs and with locomotion speed.

Movie S2. Example two-photon calcium imaging recording with visual stimulation

Example recording showing a field of view with four ChCs (red and encircled) and PyCs during spontaneous behavior and visual stimulation (moving gratings, indicated as 'Visual stimulus' at the top right of the field of view). The activity of the four ChCs is shown on the right as red traces. Movie frames correspond to the ΔF/F values at the dotted line. The black trace (bottom right) indicates the running speed of the mouse. Playback speed is 2x real time. Note the visual responses of both ChCs and PyCs.

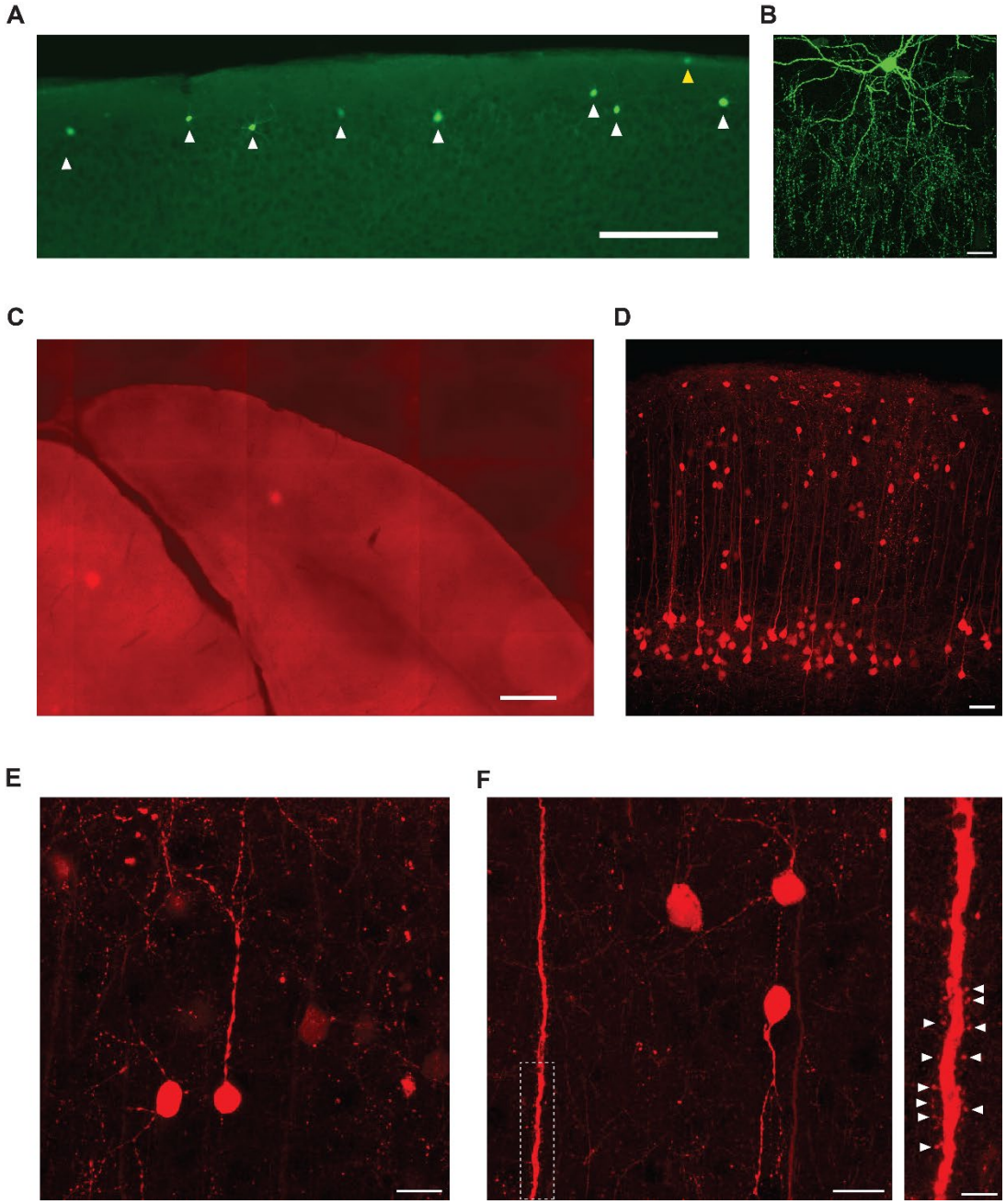

Figure S1. Morphology of labeled ChCs and putative GABAergic input neurons in L2/3

(A) Confocal image of superficial V1 with eYFP-TVA-labeled neurons in Vipr2-cre mice. White arrows indicate ChCs, the yellow arrow indicates a non-ChC in L1. Labeled cells were denoted as ChCs based on their location on the border between L1 and L2/3 and their dendritic and axonal morphology. Scale bar, 200 µm.

(B) Confocal z-stack (0.25 µm sections) max projection of an example ChC with distinctive dendritic and axonal morphology. Scale bar, 20 µm.

(C) Overview of V1 from a control mouse where no labeled cells were detected. Scale bar, 400 µm.

(D) Confocal overview image showing dense PyC labeling in L5 and sparse distributed labeling in layers 1 to 4. Scale bar, 50 µm.

(E) High magnification confocal image of L2/3 neurons showing round non-pyramidal morphology. Scale bar, 10 µm.

(F) Left: high magnification confocal image of L2/3 neurons and a L5 apical dendrite containing spines. Inset: zoomed in confocal image of the dotted region showing individual spines (white arrows) on the L5 apical dendrite. Scale bar, 10 µm and 5 µm (inset).

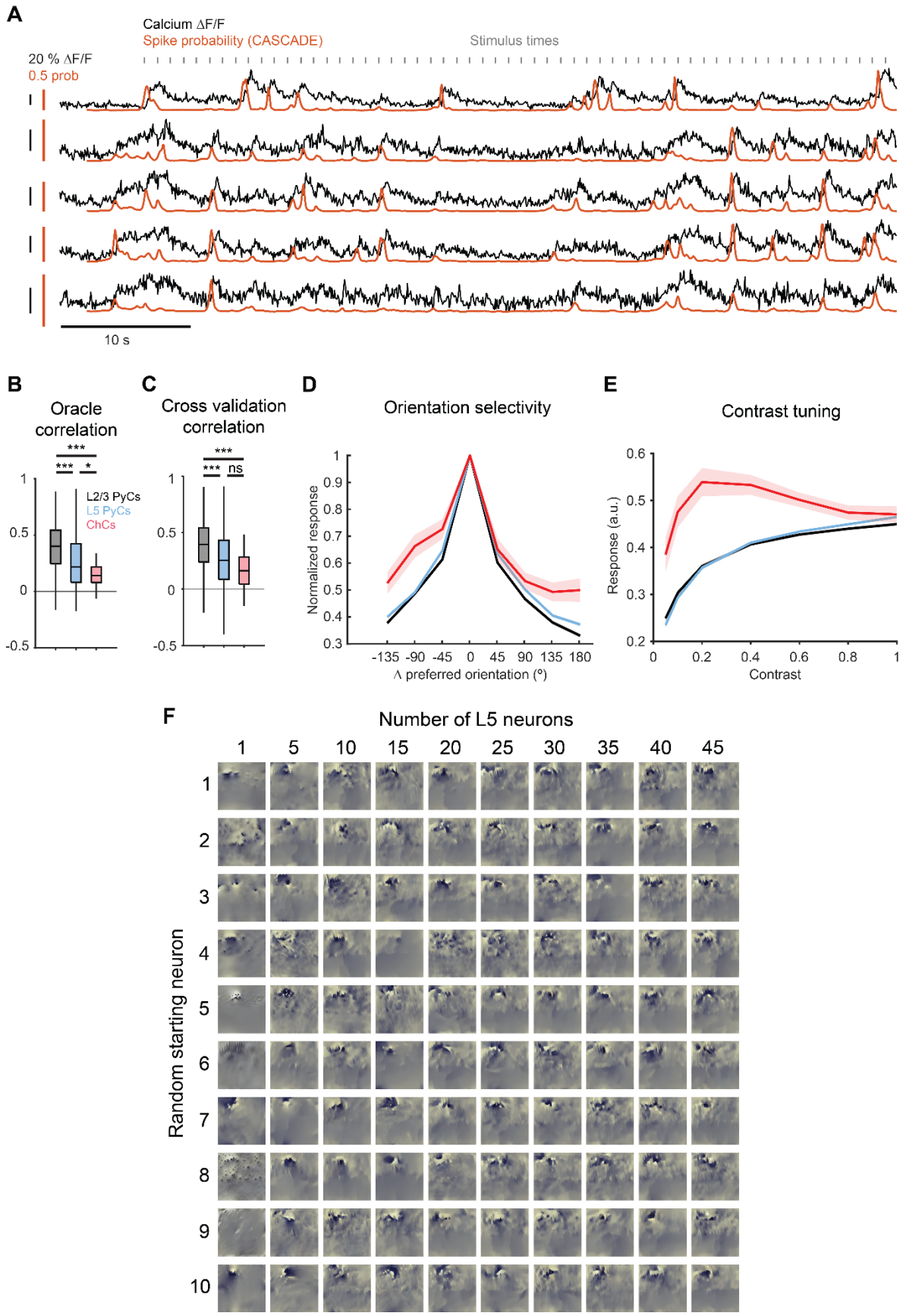
A
Calcium ΔF/F
Spike probability (CASCADE)
Stimulus times
20 % ΔF/F
0.5 prob
10 s
B
Oracle correlation
L2/3 PyCs
L5 PyCs
ChCs
C
Cross validation correlation
ns
D
Orientation selectivity
Normalized response
Λ preferred orientation (°)
E
Contrast tuning
Response (a.u.)
Contrast
F
Number of L5 neurons
Random starting neuron

Figure S2. CNN model performance and tuning curves obtained from CNN predictions

(A) Traces of 5 example ChCs showing ΔF/F (black) and spike probability (red) obtained using CASCADE. Gray indicators show stimulus times of natural images.

(B) Average oracle correlation for each cell type. ChCs show lower oracle correlations than L2/3 PyCs and L5 PyCs. LMEM for all comparisons, ***: $p < 0.001$, * $p < 0.05$, ns: not significant. Box plots represent median, quantiles and 95% confidence interval (CI) over neurons.

(C) Average cross validation correlation for each cell type. ChCs and L5 PyCs show lower cross validation correlations than L2/3 PyCs. Cross validation correlations were comparable to oracle correlations (maximally achievable correlations), indicating high performance of the CNN model for all cell types.

(D) Orientation tuning curves for each cell type. Curves represent mean +- SEM over neurons after aligning single cell curves to their preferred orientation. Data are normalized to the max response for each cell.

(E) Contrast tuning curves for each cell type. Note the weak tuning of ChCs for contrast.

(F) L5 MEIs obtained by optimizing responses from combinations of L5 PyCs. Each row represents a different starting L5 PyCs, with increasing numbers of L5 PyCs added to the optimization from left to right. Note the decrease in structure with increasing numbers of L5 PyCs used.

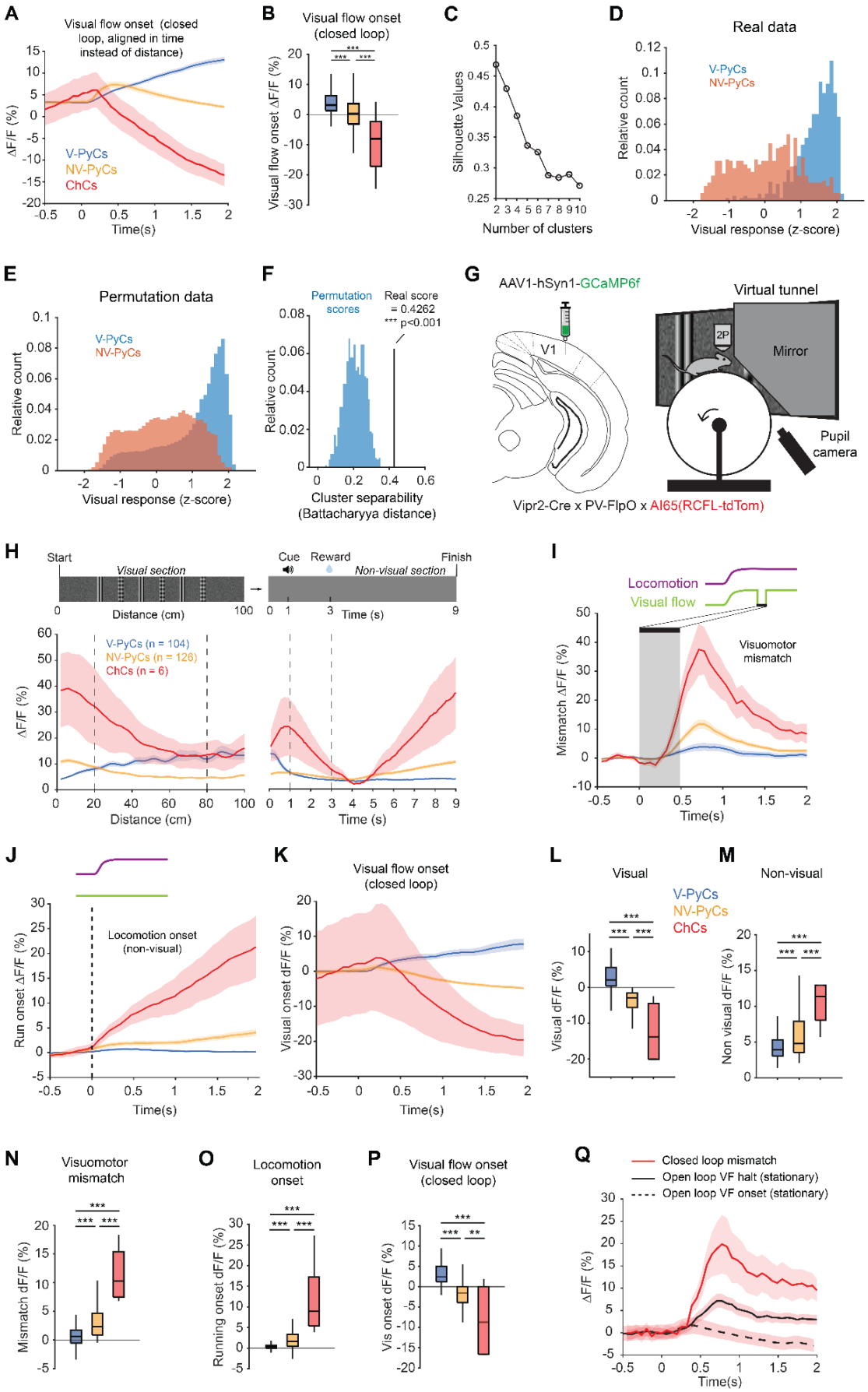
A
Visual flow onset (closed loop, aligned in time instead of distance)
ΔF/F (%)
V-PyCs
NV-PyCs
ChCs
Time(s)
B
Visual flow onset (closed loop)
Visual flow onset ΔF/F (%)
C
Silhouette Values
Number of clusters
D
Real data
Relative count
V-PyCs
NV-PyCs
Visual response (z-score)
E
Permutation data
Relative count
V-PyCs
NV-PyCs
Visual response (z-score)
F
Permutation scores
Real score = 0.4262
*** p<0.001
Relative count
Cluster separability (Battacharyya distance)
G
AAV1-hSyn1-GCaMP6f
V1
Virtual tunnel
2P
Mirror
Pupil camera
Vipr2-Cre x PV-FlpO x Ai65(RCFL-tdTom)
H
Start
Visual section
Cue
Reward
Finish
Non-visual section
Distance (cm)
Time (s)
V-PyCs (n = 104)
NV-PyCs (n = 126)
ChCs (n = 6)
ΔF/F (%)
Distance (cm)
Time (s)
I
Locomotion
Visual flow
Visuomotor mismatch
Mismatch ΔF/F (%)
Time(s)
J
Locomotion onset (non-visual)
Run onset ΔF/F (%)
Time(s)
K
Visual flow onset (closed loop)
Visual onset dF/F (%)
Time(s)
L
Visual
V-PyCs
NV-PyCs
ChCs
Visual dF/F (%)
M
Non-visual
Non visual dF/F (%)
N
Visuomotor mismatch
Mismatch dF/F (%)
O
Locomotion onset
Running onset dF/F (%)
P
Visual flow onset (closed loop)
Vis onset dF/F (%)
Q
Closed loop mismatch
Open loop VF halt (stationary)
Open loop VF onset (stationary)
ΔF/F (%)
Time(s)

Figure S3. Open loop and PV$^+$ ChC responses

(A) Average population activity during visual flow onset in closed loop experiments from Fig. 4. Traces are aligned to start of the tunnel rather than distance along the tunnel. Traces represent mean +- SEM over neurons.

(B) Average activity during visual flow onset in closed loop. LMEM-Tukey for all comparisons, ***p<0.001.Box plots represent median, quantiles and 95% confidence interval (CI) over neurons.

(C) Silhouette analysis of PyC clustering. Clustering with a cluster number of two resulted in highest silhouette values.

(D) Histogram distributions of visual response magnitude for V-PyCs and NV-PyCs on the real data from Fig 4. Responses were calculated by averaging activity between 20-80 cm on z-scored traces over the entire virtual tunnel.

(E) Histogram distributions as described in D), but for permutation data. Visual responses were calculated as in D), but on traces obtained from shuffling the visual and nonvisual section traces across neurons.

(F) Histogram showing the cluster separability calculated as Battacharyya distance for the permutation data (blue histogram) and the real distribution (black line). Real separability is higher than expected by chance. Permutation test, ***p<0.001.

(G) Schematic of approach for PV$^+$ ChCs. ChCs were identified using Cre- and Flippase-dependent expression of tdTom (AI65 mouse line) in Vipr2-Cre x PV-FlpO mice.

(H) Average population traces of V-PyCs, NV-PyCs and ChCs in the visual (left) and non-visual (right) part of the tunnel (230 PyCs and 6 ChCs, 2 sessions from 2 mice). PV$^+$ ChCs follow the activity profile of NV-PyCs.

(I) Average population traces during visuomotor mismatch events.

(J) Average population traces at locomotion onset in the non-visual part of the tunnel.

(K) Average population traces during visual flow onset in closed loop experiments. Traces are aligned to start of the tunnel rather than distance along the tunnel.

(L) Average activity during visual stimuli (20-80 cm) compared to start of tunnel (0-20 cm).

(M) As in L, but for activity in the entire non-visual part of the tunnel.

(N) As in L, but for visuomotor mismatch events.

(O) As in L, but for locomotion onset events.

(P) As in L, but for visual flow onset events.

(Q) Average population traces comparing closed loop mismatch with open loop VF halt and open loop VF onset when the mice were stationary (related to Fig. 4).